Invariance, groups, and non-uniqueness: The discrete case

D. W. Vasco
Berkeley Laboratory, University of California, Berkeley, California

Short title: INVARIANCE, GROUPS, AND NON-UNIQUENESS

Abstract.

Lie group methods provide a valuable tool for examining invariance and non-uniqueness associated with geophysical inverse problems. The techniques are particularly well suited for the study of non-linear inverse problems. Using the infinitesimal generators of the group it is possible to move within the null space in an iterative fashion. The key computational step in determining the symmetry groups associated with an inverse problem is the singular value decomposition (SVD) of a sparse matrix. I apply the methodology to the eikonal equation and examine the possible solutions associated with a crosswell tomographic experiment. Results from a synthetic test indicate that it is possible to vary the velocity model significantly and still fit the reference arrival times. The approach is also applied to data from crosswell surveys conducted before and after a CO_2 injection at the Lost Hills field in California. The results highlight the fact that a fault cross-cutting the region between the wells may act as a conduit for the flow of water and CO_2.

Introduction

Geophysical inverse problems rarely have unique solutions. Typically, uniqueness is bestowed upon an inverse problem through the introduction of specific biases, 'prior' information, or penalty terms (Jackson 1979, Tarantola 1987, Parker 1994). Such biases stabilize the inverse problem and provide a seemingly unique solution. However, the solution now depends on the nature of the 'prior' information, thus trading one form of non-uniqueness for another.

The non-uniqueness of solutions to geophysical inverse problems has been recognized for some time. A number of methods have been developed to quantify the range of possible solutions. Rather complete treatments exist for linear inverse problems. The early treatment by Backus and Gilbert (1968, 1970) and others (Jackson 1972, Wiggins 1972) emphasized the non-uniqueness inherent in the majority of geophysical inverse problems and the averaging nature of model parameter estimates. For linear problems, non-uniqueness has been characterized by model parameter covariances (Tarantola 1987, Parker 1994) as well as by bounds (Backus 1970, Parker 1974, Sabatier 1977, Safon et al. 1977) or confidence intervals (Backus 1989, Stark 1992) on model parameters. Furthermore, techniques which make use of the null-space associated with a linear inverse problem may be used to incorporate *a priori* information without influencing the fit to the data (Deal and Nolet 1996, Rowbotham and Pratt 1997).

For non-linear inverse problems the characterization of non-uniqueness is more difficult due to the presence of local minima. Hence, it is generally not possible to guarantee that the non-uniqueness has been completely quantified, and one must rely on approximations and/or iterative methods. For example the methods of Backus and Gilbert (1968, 1970), can be applied to non-linear inverse problems using an iterative perturbation approach. Alternatively, it may be possible to transform a non-linear inverse problem into a linear problem using either statistical or algebraic means (Vasco 1995, 1997). Techniques from linear inverse theory may then be applied in the transformed space in order to quantify non-uniqueness. For discrete inverse problems several statistical sampling-based methods, such as Monte Carlo search (Press 1968) or its extensions (Mosegaard and Tarantola 1995, Sambridge 1998), have been proposed to examine non-uniqueness. A different approach by Vasco (1999, 2000) makes use of techniques from computational algebra to characterize the solutions to non-linear geophysical inverse problems.

There is a need for general and robust techniques for exploring the null space associated with a non-linear geophysical inverse problem. In particular, it would be useful to have the ability to move about the space of model parameters and yet stay within the null space. It would be especially advantageous to have the ability of moving within the null space in a direction which minimizes or maximizes some attribute of the

model such as roughness. In this paper I introduce a method for moving within the null space that is based upon Lie groups. Lie groups are continuous groups that have proven useful in a variety of contexts, particularly in applications to non-linear problems (Olver 1986, Bluman and Kumei 1989, Euler and Steeb 1992). The technique developed here is very general and only requires the singular value decomposition (SVD) of a sparse matrix. The method generalizes the approach of Deal and Nolet (1996) and Rowbotham and Pratt (1997) for linear inverse problems.

I apply the methodology to a set of governing equations for first-arrival time tomography. Both velocity and the travel time fields for all of the sources are treated as unknowns. This provides insight into the nature of the non-uniqueness associated with the inverse problem. The application to field data from the Lost Hills, California indicates that the technique works in the presence of noise. I must emphasize that the technique is applicable to the normal equations resulting from a least squares formulation. Symmetry groups may also be useful in stochastic formulations of inverse problems. In particular, Lie groups may be used to examine invariance and symmetry associated with probability density functions. Another advantage of Lie groups is that they may be used to treat continuous problems in the form of differential and integral equations (Olver 1986). For example, in Vasco (1997) Lie groups are used to determine if an inverse problem involving non-linear functionals may be transformed into a linear inverse problem.

Methodology

In this section I briefly define Lie groups and indicate how they are used to transform a vector of model parameters. The notion of symmetry is defined, as are the ideas of infinitesimal invariance and Lie vector fields. The final result is a set of conditions for a Lie group to be a symmetry group of a system of equations. That is, conditions such that a transformed model stays within the solution set.

Non-uniqueness and invariance

Consider a set of l equations

$$F^i(\mathbf{x}) = 0, \quad i = 1, ..., l \tag{1}$$

where $\mathbf{x} \in M \subset R^n$ is a vector of unknowns, and the $F^i(\mathbf{x})$ are smooth real-valued functions of $\mathbf{x}$. I am interested in transformations which leave the solution set of the equations invariant. Note that this is not the same as leaving the functions themselves invariant. Groups, in particular the Lie groups I discuss below, are a useful tool in the study of invariance.

Invariance and groups

For the study at hand, the most relevant groups are those which 'act' on sets of objects, the transformation groups:

Definition A *transformation group* is a continuous group S and a set $M \subset R^n$ along with a smooth map $\Psi : S \times M \to M$ which satisfies, for $s, t \in S, \mathbf{x} \in M$,

$$\Psi(s, \Psi(t, \mathbf{x})) = \Psi(s \cdot t, \mathbf{x}), \tag{2}$$

and contains an identity element e such that

$$\Psi(e, \mathbf{x}) = \mathbf{x}, \tag{3}$$

and an inverse element s^{-1}

$$\Psi(s^{-1}, \Psi(s, \mathbf{x})) = \mathbf{x}. \tag{4}$$

It turns out that the group properties (2), (3), and (4), together with continuity requirements on the multiplication and inversion operations, provide enough algebraic structure for the study of invariance or symmetry (Gilmore 1974).

Definition A group of transformations acting on a set $M \subset R^n$, S is called a symmetry group of M, if whenever $\mathbf{x} \in M$ and $s \in S$ then $\Psi(s, \mathbf{x}) \in M$.

The set M is said to be invariant with respect to the actions of the group. In cases of interest the set M is defined by the vanishing of l equations. Such sets are known as the zero set or the variety of the system of equations (1).

Infinitesimal invariance and Lie vector fields

The great utility of continuous groups rests upon a form of linearization. This type of linearization is different from one about a particular value of $\mathbf{x}$. Rather, I linearize with respect to the group element s, about the identity transformation e. The importance of this linearization cannot be over-emphasized. It allows one to transform complicated non-linear invariance conditions on the group to linear equations. Furthermore, because the linearization is about the group parameters and not about particular values of the variables, the conditions are applicable to the entire range of solutions.

To illustrate the main ideas, I shall examine a one parameter group of transformations

$$\mathbf{x}' = \Psi(\varepsilon, \mathbf{x}), \tag{5}$$

where the scalar ε represents the group parameter. One can construct multi-parameter groups from one-parameter components (Olver 1986, Bluman and Kumei 1989).

Consider a Taylors expansion of $\Psi(\varepsilon, \mathbf{x})$ in ε, about $\varepsilon = 0$,

$$\Psi^j(\varepsilon, \mathbf{x}) = \mathbf{x}^j + \varepsilon \xi^j(\mathbf{x}) + \cdots. \tag{6}$$

The partial derivative of the transformed variable with respect to a change in ε at $\varepsilon = 0$ (at the identity transformation), is denoted by $\xi^j(\mathbf{x})$:

$$\frac{\partial \Psi^j(\varepsilon, \mathbf{x})}{\partial \varepsilon}|_{\varepsilon=0} = \xi^j(\mathbf{x}). \tag{7}$$

The Taylor series expansion, given in equation (6), is equivalent to a repeated application of a differential operator derived from $\xi(\mathbf{x})$ (Bluman and Kumei 1989, p. 41)

$$\mathbf{X}_x = \frac{\partial \Psi^j(\varepsilon, \mathbf{x})}{\partial \varepsilon}|_{\varepsilon=0} \frac{\partial}{\partial x^j} = \xi^j(\mathbf{x}) \frac{\partial}{\partial x^j} \tag{8}$$

where the summation convention, summation over repeated indices, has been employed. Mathematically, the vector field $\mathbf{X}_x$ is a differential operator which acts on a function to give the rate of change of the function in the direction specified by the components $\xi^j(\mathbf{x})$. That is, along the flow of the mapping, as parameterized by ε. Thus, I may write the Taylors expansion of $\Psi(\varepsilon, \mathbf{x})$ as

$$\begin{aligned} \Psi(\varepsilon, \mathbf{x}) &= \mathbf{x} + \varepsilon \mathbf{X}_x \mathbf{x} + \frac{\varepsilon^2}{2} \mathbf{X}_x \mathbf{X}_x \mathbf{x} + \cdots \\ &= \left[\sum_{k=0}^{\infty} \frac{\varepsilon^k}{k!} \mathbf{X}_x{}^k \right] \mathbf{x} \end{aligned} \tag{9}$$

The infinite sum in brackets, known as a Lie series, is often denoted symbolically by $\mathrm{EXP}(\varepsilon \mathbf{X}_x)$ (Gilmore 1974). Equation (9) suggests that the operator $\mathbf{X}_x$ contains all the information concerning the transformation. Because of this, $\mathbf{X}_x$, known as the infinitesimal generator or Lie vector, forms the basis for studying invariance with respect to such transformations. In particular, the conditions for the group to leave M invariant may be written in terms of $\mathbf{X}_x$.

Theorem 1 *Let S be a Lie group of transformations acting on the m-dimensional set $M \subseteq R^n$. Let $F : M \to R^l, l \leq m$ define a system of equations*

$$F^i(\mathbf{x}) = 0, \quad i = 1, ..., l. \tag{10}$$

Then S is a symmetry group of the system if and only if

$$\mathbf{X}_x[F^i(\mathbf{x})] = 0, \quad , i = 1, ..., l \tag{11}$$

whenever $F^i(\mathbf{x}) = 0$, $i = 1, ..., l$ for every infinitesimal generator $\mathbf{X}_x$ of S.

This theorem follows by applying $\mathrm{EXP}(\varepsilon \mathbf{X}_x)$ in equation (9) to $F^i(\mathbf{x})$ (Bluman and Kumei 1989). As demonstrated below, this theorem means that complicated non-linear conditions for invariance may be replaced by a linear system of equations.

Application

Travel-time tomography

Governing Equations

In this section I consider the non-uniqueness associated with travel-time tomography. I will illustrate the Lie group approach in a crosswell tomographic setting, as shown in Figure 1. A seismic source is moved, in succession, to five positions in left-most borehole [denoted by stars]. At each position the source is activated and the resulting seismic wavefield is recorded by 14 receivers in the borehole on the right [denoted by filled squares].

The starting point is the eikonal equation describing the evolution of the travel time (Aki and Richards 2002, page 87). In all that follows I shall denote the travel time field associated with source l by $u^l(\mathbf{r})$, a function of position $\mathbf{r}$ in the Earth. For a source l the following constraints apply

$$\nabla u^l(\mathbf{r}) \cdot \nabla u^l(\mathbf{r}) - \sigma(\mathbf{r}) = 0 \tag{12}$$

$$u^l(\mathbf{r}_{m_l}) = T^l{}_{m_l} \qquad m_l = 1, ..., M_l \tag{13}$$

where the variable $\sigma(\mathbf{r})$ represents the reciprocal of the square of the velocity or the square of the slowness, which is also a function of position, m_l denotes the receiver number, and $\mathbf{r}_{m_l}$ is the position of receiver number m_l. For source l there are a total of M_l receivers, a number which will generally vary for each source. Note that one should also include the source point as a zero travel time constraint, a boundary condition for the eikonal equation. Thus, the source point introduces another constraint of the form (13).

I must emphasize that, in addition to the unknown slowness distribution between the boreholes, the travel time fields between the wells (Figure 2) are also unknown. Usually, the travel time field associated with each source is considered to be a function of the slowness field. However, strictly speaking, both the travel time and slowness fields are unknowns in the inverse problem. The unknown slowness and each travel time field are constrained by the eikonal equation (12) and the arrival times measured at the receivers (13). It is true that, given the slowness field I can use the eikonal equation (12) to compute the travel time variation between the boreholes. But, it is equally true that, given the travel time distribution between the wells I can use the eikonal equation to find the slowness. Figure 3 illustrates the fact that, by computing the gradient of the travel time field, calculating its magnitude, and taking the square root, I can determine the slowness variation. In what follows I include the travel time fields as explicit unknowns in the inverse problem. While this necessitates additional computation, it provides important insight into the nature of the non-uniqueness associated with the inverse problem.

The Discrete Problem

In this paper I shall consider the discrete inverse problem, described by a finite number of parameters. Before I derive the symmetry group generators I first write equations (12) and (13) as a discrete system of equations. The nl-th constraint associated with the eikonal equation (12) is given by

$$\Theta_n{}^l = \Delta_n u_n{}^l \cdot \Delta_n u_n{}^l - \sigma_n = 0 \tag{14}$$

where $n = 1, ..., N$ signifies one of the N grid points, Δ_n is a finite difference approximation to the gradient, and $l = 1, ..., L$, for L sources. For receiver number m_l and source l, the data and source boundary constraints are

$$\Omega_{m_l}{}^l = u_{m_l}{}^l - T_{m_l}{}^l = 0 \tag{15}$$

with $m_l = 1, ..., M_l + 1$. Note that, as each additional source is introduced, one gains N constraints from the eikonal equation and M_l constraints from the travel time observations at the receivers. There may also be a number, say N_b, of boundary constraints on the slowness. For example, well logs might be used to fix the velocity near the borehole wall. The total number of equations, N_{eq} is given by the sum

$$N_{eq} = N \cdot L + \sum_{l=1}^{L} M_l + L + N_b. \tag{16}$$

However, because an additional travel time field $\mathbf{u}^l$ is associated with each new source, I also add N new variables to the set of unknowns. Thus, the total number of unknowns is

$$N_u = N \cdot (L + 1) \tag{17}$$

and the inverse problem is formally over-determined when $\sum_{l=1}^{L} M_l + L + N_b$ exceeds N.

The variables for the tomographic inverse problem, the components of $\mathbf{x}$, are the square of the slowness in each grid block σ_n and the travel time for each source in each grid block, $u_n{}^l$. Thus, I may write the vector of model parameters $\mathbf{x}$ as a composite vector $(\sigma, \mathbf{u}^1, ..., \mathbf{u}^L)$. The Lie vector $\mathbf{X}_x$ is written in the partitioned form $\mathbf{X}_{\sigma,u}$

$$\mathbf{X}_{\sigma,u} = \mu^n \frac{\partial}{\partial \sigma_n} + \xi^{nl} \frac{\partial}{\partial u_n{}^l} \tag{18}$$

where I have invoked the convention of summing over repeated indices.

Estimating group parameters using the SVD

I wish to characterize the transformation group which will allow me to vary the model parameters and still satisfy the constraint equations. In what follows I will not

explicitly include the boundary conditions on σ_n. As stated in Theorem 1, the condition for $\mathbf{X}_{\sigma,u}$ to generate the symmetry group for the inverse problem is that $\mathbf{X}_{\sigma,u}{\Theta_n}^l$ and $\mathbf{X}_{\sigma,u}{\Omega_{m_l}}^l$ vanish. Applying $\mathbf{X}_{\sigma,u}$ to the eikonal constraint ${\Theta_n}^l$, given by (14), results in a linear equation in ${\xi_n}^l$ and μ_n

$$2\Delta_n {u_n}^l \cdot \Delta_n {\xi_n}^l - \mu_n = 0 \tag{19}$$

for $n = 1, ..., N$ and $l = 1, ..., L$. Similarly, applying $\mathbf{X}_{\sigma,u}$ to the data constraint ${\Omega_{m_l}}^l$, equation (15), results in

$${\xi_{m_l}}^l = 0 \tag{20}$$

where $m_l = 1, ..., M_l$.

I can rewrite the two sets of equations (19) and (20) as a single matrix-vector equation

$$\mathbf{P}\boldsymbol{\Upsilon} = \mathbf{0} \tag{21}$$

where I have defined the vector of coefficients $\boldsymbol{\Upsilon} = (\vec{\mu}, \vec{\xi}_1, \ldots, \vec{\xi}_L)$ and the matrix $\mathbf{P}$

$$\mathbf{P} = \begin{bmatrix} -\mathbf{I} & \mathbf{D}_1 & \ldots & \mathbf{0} & \mathbf{0} \\ \mathbf{0} & \mathbf{T}_1 & \ldots & & \mathbf{0} \\ \vdots & & \ddots & & \vdots \\ -\mathbf{I} & & \ldots & \mathbf{0} & \mathbf{D}_L \\ \mathbf{0} & \mathbf{0} & \ldots & \mathbf{0} & \mathbf{T}_L \end{bmatrix}. \tag{22}$$

In the matrix $\mathbf{P}$, the sub-matrices $\mathbf{T}_l$ contain the coefficients corresponding to the data constraints (20). Similarly, the sub-matrices $\mathbf{D}_l$ contains coefficients corresponding to the first term in equation (19), and $\mathbf{I}$ is the identity matrix.

I will treat the situation when there are fewer constraints than unknowns, that is, the quantity $\sum_{l=1}^{L} M_l + L + N_b$ is less than N. Thus, the system of equations is formally under-determined and has an infinite number of solutions. Equivalently, the matrix (22) is rectangular and has fewer rows than columns. In this case there will be a non-trivial null-space which characterizes the non-uniqueness. The singular value decomposition (SVD) (Noble and Daniel 1977) is perhaps the most reliable technique for calculating the vectors in the null-space and extracting its dimension. The SVD is a representation of the matrix $\mathbf{P}$ as the product of three matrices

$$\mathbf{P} = \mathbf{U}\boldsymbol{\Lambda}\mathbf{V}^T \tag{23}$$

where $\mathbf{U}$ is an $N_{eq} \times N_{eq}$ matrix with orthogonal columns, $\mathbf{V}^T$ is an $N_u \times N_u$ orthogonal matrix, and $\boldsymbol{\Lambda}$ is an $N_{eq} \times N_u$ diagonal matrix, which is of the form

$$\boldsymbol{\Lambda} = \begin{bmatrix} \lambda_1 & & \ldots & & 0 & \ldots & 0 \\ 0 & \lambda_2 & & & & & \\ \vdots & & \ddots & & & & \vdots \\ 0 & & \ldots & \lambda_p & 0 & \ldots & 0 \end{bmatrix}. \tag{24}$$

The scalars λ_i are ordered such that $\lambda_1 \leq \lambda_2 \leq ... \leq \lambda_{p-1} \leq \lambda_p$. The integer p denotes the actual dimension of the problem, which may be less then N_{eq} due to degeneracy. The integer $N_u - p$ characterizes the dimension of the null-space. That is, values of λ_i which are near zero indicate vectors which are effectively in the null-space and should be treated as such.

In Figure 4 I have plotted the singular values associated with the crosswell illustration. For this example the region between the boreholes is sub-divided into a 13 (horizontal) by 25 (vertical) grid, a total of 325 grid-blocks. The unknown parameters are the slowness values for each grid block and the travel time values for each source at each node of the grid. Thus, I have a total of 1950 model parameters in this test case. The model parameters are constrained by 1781 equations which are provided by the eikonal equation for each source, the travel time constraints, and boundary constraints at the wells. Hence, there is a 169 dimensional null-space, representing the non-uniqueness inherent in the inverse problem. The null-space vectors are associated with the zero singular values in Figure 4. As additional sources are added the dimension of the null-space will decrease. However, if the source and receiver positions are similar to a previous source-receiver geometry, the additional constraints are essentially redundant. In that case, a nearly zero singular value occurs, signifying an almost singular system of equations.

Selected singular vectors $\mathbf{v}_i$, which are column vectors of the matrix $\mathbf{V}$, are plotted graphically in Figures 5, 6, and 7. Figure 5 displays the vectors associated with the 1st, 6th, and 25th largest singular values (λ_1, λ_6, and λ_{25}). The components of the vector $\mathbf{v}_i$ associated with the first source ($\mathbf{u}_1$) and the squared slowness ($\vec{\sigma}$) are plotted in the locations of the corresponding grid-blocks. The grey scale plots in Figures 5 and 6 show the amplitude of the components. The patterns represent those combinations of the components of $\vec{\xi}_1$ and $\vec{\mu}$ which are well constrained by the system of linear equations (21). The combinations are averages of the components which lie between the source location and the various receivers. In Figure 6, I have plotted the components associated with the first, third, and fifth shot points. The vectors $\mathbf{v}_i$ in Figure 6 correspond to the largest singular value. Note how the pattern of averaging shifts as the source location is changed.

The components of $\mathbf{v}_i$ associated with the 1st, 50th, and 100th null vectors are plotted in Figure 7. That is, these three vectors lie in the null space, signified by $\lambda_i = 0$. Hence, these combinations of components of $\vec{\xi}$ and $\vec{\mu}$ not constrained by equation (21) and may vary arbitrarily. The averaging appears to include particular cells in the interior of the crosswell region and a significant number of cells near the upper edge of the region. The upper edge of the region between the wells in not constrained by seismic energy, as is evident from the source-receiver distribution in Figure 1. As shown next, it is the vectors $\mathbf{v}_i$ associated with zero singular values which define permissible movement

within the model space.

Movement within the null-space

In this sub-section I will let x_i denote the ith model parameter and I shall not distinguish between slowness and travel time field variables. Based upon the SVD I can write $\mathbf{X}_x$ in the partitioned form

$$\mathbf{X}_x = \mathbf{X}_x{}^g + \mathbf{X}_x{}^0 \tag{25}$$

where $\mathbf{X}_x{}^g$ is computed using the generalized inverse (Aki and Richards, 2002) and $\mathbf{X}_x{}^0$ is a vector in the null-space. That is, a vector of the form

$$\mathbf{X}_x{}^0 = \sum_{i=p+1}^{N_u} a_i \sum_{j=1}^{N_u} v_j{}^i \frac{\partial}{\partial x_j} \tag{26}$$

where a_i is an arbitrary multipiler, and $v_j{}^i$ is the jth component of the ith column vector of $\mathbf{V}$. Because the right-hand-side of (21) is zero, $\mathbf{X}_x{}^g$ is also zero. This is clear because $\mathbf{X}_x{}^g$ is simply the generalized inverse, a matrix, multiplied by the right-hand-side of (21) which is the zero vector.

The Lie vector $\mathbf{X}_x$ may be used to move through the null-space. Specifically, I can use equation (9) to transform the current model $\mathbf{x}$ to a new model. It will be assumed that ε is small so that terms of order ε^2 and greater may be neglected. I will denote the new model by a prime, thus

$$\mathbf{x}' = \mathbf{x} + \varepsilon \mathbf{X}_x{}^0 \mathbf{x} \tag{27}$$

to order ε. Applying $\mathbf{X}_x{}^0$ to $\mathbf{x}$ gives

$$\mathbf{X}_x{}^0 \mathbf{x} = \sum_{i=p+1}^{N_u} a_i \sum_{j=1}^{N_u} v_j{}^i \frac{\partial \mathbf{x}}{\partial x_j}. \tag{28}$$

Because

$$\frac{\partial x_k}{\partial x_j} = \delta_k{}^j, \tag{29}$$

where $\delta_k{}^j$ is the Kroniker delta function which is 1 when $k = j$ and 0 when $k \neq j$, I may write equation (27) as

$$\mathbf{x}' = \mathbf{x} + \varepsilon \sum_{i=p+1}^{N_u} a_i \mathbf{v}^i. \tag{30}$$

Equation (30) allows one to move to a new model $\mathbf{x}'$ while remaining within the solution set. By varying the coefficients a_i I can generate various models which satisfy the constraints. The issue now is to find models which are of particular interest. For example, to move toward models which satisfy the data but are smoother than the

current model, or models which are closer to a preferred structure, In this section and the next, I will consider the latter case, denoting the preferred model parameter vector by $\mathbf{\Pi}$. The goal is to move towards $\mathbf{\Pi}$ while remaining within the solution set. To this end, I define a functional $R(\mathbf{a})$, which provides a measure of the distance between $\mathbf{x}'$ and Π

$$R(\mathbf{a}) = (\mathbf{x}' - \mathbf{\Pi})^T \cdot (\mathbf{x}' - \mathbf{\Pi}) \tag{31}$$

which is a function of the coefficients a_i in equation (30). Geometrically, the direction in which one should move in order to minimize $R(\mathbf{a})$ is the projection of $\nabla R(\mathbf{a})$ onto the null-space. That is, the projection of $\mathbf{x} - \mathbf{\Pi}$ onto the basis vectors $\mathbf{v}^i$ in equation (30). Thus, $a_i = \mathbf{n} \cdot \mathbf{v}^i$ where $\mathbf{n} = (\mathbf{x} - \mathbf{\Pi})/|\mathbf{x} - \mathbf{\Pi}|$ is the unit vector in the direction of $\mathbf{x} - \mathbf{\Pi}$. In terms of $\mathbf{n}$, equation (30) becomes

$$\mathbf{x}' = \mathbf{x} + \varepsilon \sum_{i=p+1}^{N_u} \left(\mathbf{n} \cdot \mathbf{v}^i\right) \mathbf{v}^i. \tag{32}$$

The procedure for moving towards the model $\mathbf{\Pi}$ involves the repeated updating of $\mathbf{x}$, as given in equation (32). For each update, the vectors $\mathbf{v}_i$ are recomputed based upon an SVD of the matrix $\mathbf{P}$, given in equation (22). The matrix $\mathbf{P}$ must be recalculated at each iteration due to the change in the model following an update. Note that when the vectors defining the null-space motion, $\mathbf{v}_i$, are orthogonal to $\mathbf{n}$ the updates cease to be significant. Geometrically, the 'tangent plane' to the null-space is perpendicular to the vector $\nabla R(\mathbf{a})$.

I illustrate the technique with an application to the crosswell problem described above (Figure 1). In this case I wish to find a model which satisfies the data yet is closest to a homogeneous model. The homogeneous model has a constant slowness of 0.61 s/km. Starting with the model in Figure 1 I compute the group parameters based upon the SVD of $\mathbf{P}$, as in equation (23). The model is then updated according to equation (32) where $\mathbf{\Pi}$ is the constant slowness model. The method is iterative, at each stage a new model $\mathbf{x}'$ is derived using equation (32) with $\varepsilon = 0.1$. The value of the function $R(\mathbf{a})$, given by equation (31), as a function of the number of iterations is shown in Figure 8. Note that, after about ten iterations, the decrease in $R(\mathbf{a})$ levels off as $\mathbf{v}_i$ becomes orthogonal to $\nabla R(\mathbf{a})$ and the coefficients in the summation (32) approach zero. The value of $R(\mathbf{a})$ is reduced to less than 30% of its original value in sixteen iterations.

In Figure 9 four models are displayed, corresponding to various stages of the iterative algorithm. The range in models is rather remarkable. As expected, the overall amplitude variation from the background slowness of 0.61 s/km decreases with the number of iterations. Similarly, the spatial variation in slowness becomes generally smoother as the iterations proceed. However, some small amplitude heterogeneity which varies rapidly in space is super-imposed on a smoothly varying background in the 16th

iteration. It is interesting that the high amplitude, low-slowness region, located around a depth of 7.2 m, migrates downward and out of the model. At the 4th iteration it lies at a depth of 8 m and by the 8th iteration it is found at a depth of 9 m. In the final model the low-slowness zone is no longer present.

Data misfit at four steps of the algorithm are shown in Figure 10. The misfit is associated with the models in Figure 9. In general there is a slight degradation at the iterations proceed. This is due to numerical noise associated with each iteration. First, only zero singular values were used in the sum (30). Very small amplitude singular values were neglected. Second, as is evident in equation (9), the movement in the null-space is actually given as an infinite sum in ε. Thus, the linearized step of equation (30) is an approximation which introduces some errors in $\mathbf{x}'$. Thus, arrival times predicted by $\mathbf{x}'$ will contain corresponding errors. Such errors can be reduced by taking smaller iterations or by adopting a predictor-corrector scheme.

Time-lapse seismic tomography at the Lost Hills field

I apply the Lie group approach to a pair of crosswell seismic surveys at the Lost Hills oil field in southern California. The surveys were part of an experiment to determine if integrated time-lapse electromagnetic (EM) and seismic methods can be used to image saturation and pressure changes due to enhanced oil recovery (Hoversten et al. 2003). The Lost Hills reservoir is composed of diatomite, a rock with unusually high porosity (45-70%) and low permeability ($\leq$ 1 millidarcy). Production in the Lost Hills field was enhanced by hydrofracturing in the 1970s and water flooding in the 1990s. Despite these efforts , and a well spacing of only 1.25 acres, only 5% percent of the oil in place had been recovered (Gritto et al. 2004). Recently CO_2 injection was undertaken in order to improve the amount of recovered oil. Initial pilot tests were successful, improving the recovery to 56-65% of the oil in place. Even with this dramatic improvement in recovery there are production problems due to the difficulty in predicting where the CO_2 will migrate. Due to the expense of the CO_2 it is important to minimize its loss during enhanced recovery.

In order to examine the effectiveness of integrated geophysical monitoring, investigators from Berkeley Laboratory and Chevron Petroleum Company conducted pairs of seismic and EM crosswell surveys before and after the injection of CO_2. The surveys were conducted in order to image saturation and pressure changes due to the injection of the CO_2. The overall geometry of the experiments is displayed in Figure 11. The crosswell surveys were conducted in the observation wells OB-C1 and OB-C2. The two observation wells are located within a five-spot injection pattern, approximately 6 m from injection well 11-8WR (Figure 11) (Gritto 2004). The injection well was hydraulically fractured and initially water flooded from 1995 to the start of CO_2

injection in August of 2000. The CO_2 injection rate gradually increased from 3.5 to 12.0 million m^3 per day. The pressure varied between 5.5 and 6.2 MPa during the injection (Gritto 2004).

Initially, I followed a conventional approach and constructed velocity models based upon inversions of the arrival time data. The area between the observation wells was sub-divided into a 9 (horizontal) by 38 (vertical) grid of cells, in order to represent velocity heterogeneity. Five sources, and thus five travel time fields, are part of the arrival time inversion. For each source, the unknown parameters are constrained by observations from between 10 and 25 receivers, for a total of 95 arrival times. The source-receiver configuration varied between the two surveys, resulting in different ray coverage (Figure 12). The observed arrival times for the two surveys are shown in Figure 13, along with arrival times predicted using a uniform initial slowness model (0.58 s/km). While the post-injection results roughly follow the predicted linear trend of a uniform model, the observed pre-injection times increasingly deviate, as a function of offset, from the predictions.

Using a quasi-Newton iterative technique (Gill et. al. 1981) to minimize the misfit to the observed travel times, I estimated both pre- and post-injection velocity variations from the background (Figure 14). In order to regularize the inverse problem, both roughness and model norm penalties were included in the formulation (Parker 1994). The pre-injection inversion contains a high-velocity linear feature extending from the center of the right-hand-side of the crosswell region to the upper-left edge. This feature coincides with a mapped fault which traverses the crosswell region (Hoversten et al. 2003, Gritto et al. 2004). The generally higher velocity in the fault may be due to water displacing oil, a consequence of five years of water flooding. Velocities are generally lower in the lower-most half of the area between the wells. The post-injection velocity model contains a prominent low-velocity anomaly at the center-right portion of the crosswell plane.

The difference tomogram is obtained by subtracting the pre-injection velocity model from the post-injection result. The resulting velocity changes, shown in Figure 15, are dominated by the large velocity decrease in the post-injection inversion result. The velocity decrease coincides with the location of an injection interval in well 11-8WR, some six meters out of the crosswell plane. The injection interval is indicated by the large filled square in Figure 15. It is thought that a nearly vertical fracture extends from the injector to the crosswell plane.

The difference tomogram (Figure 150 indicates that a velocity decrease of over 10% is associated with the injection of CO_2. However, due to equipment changes the geometry of the two experiments, in particular the source-receiver locations and hence the ray coverage, changed significantly (Figure 12). Thus, some portion of the velocity change between the boreholes may be due to differences in survey geometry and not

simply due to changes in fluid saturation and pressure. It would be useful to estimate those changes that are required in order to match the post-injection arrival time data.

In order to determine velocity changes that are required to match the observations, I employ the methodology described above. Specifically, I begin with the model produced by an inversion of the post-injection travel time data (Figure 14b). Then, I find the model which fits the data equally well but is as close as possible to the pre-injection velocity model (Figure 14a). Thus, I employ the updating scheme of equation (32) where $\mathbf{\Pi}$ is the pre-injection slowness model (Figure 14a). A value of 0.025 is used for ε in equation (32). In 15 iterations the squared model norm $R(\mathbf{a})$ in equation (31) is reduced from 500.5 to 353.9, as shown in Figure 16. By the final iteration there is relatively little change in $R(\mathbf{a})$, as $\mathbf{n} \cdot \mathbf{v}_i$ tends to zero. The change in velocities are shown in Figure 17 for iterations 5, 10 and 15. The large amplitude, low-velocity feature in the initial post-injection result (Figure 14b) disappears. The lower-most region is characterized by lower velocities while generally higher velocities are found in the central and upper portion of the crosswell region. The low-velocity anomaly, which is notable in the fifth iteration, appears to spread downward and decrease in amplitude as the iterations proceed.

The difference tomogram is computed by subtracting the pre-injection result (Figure 14a) from the final post-injection model, the 15th iteration in Figure 17. The resulting velocity change is shown in Figure 18. Overall, the large-scale pattern of velocity change is roughly similar to the difference tomogram in Figure 15. In particular, significant velocity decrease is associated with the projection of the upper-most injection port (indicated by the largest filled square in Figures 15 and 18). Furthermore, some velocity decrease is found along what appears to be an intersecting fault in the upper-most portion of the two tomograms. However, there are two significant differences in the amplitude and the detailed spatial distribution of velocity change. First, the velocity decrease around the CO_2 injection interval has a significantly lower amplitude and is skewed to the right in the new difference tomogram. Second, the low velocity anomaly associated with the dipping fault is more significant in the new model. Note that both models fit the observations equally well (Figure 19).

Discussion and Conclusions

Faced with a non-linear inverse problem it is common practice to simply find a single solution which fits the data in some sense. The next step is to find the model parameter covariances associated with a linearization of the inverse problem. Neither quantity provides an appreciation of the true variability which is possible in the solutions satisfying the non-linear inverse problem. As shown in this paper, for under-determined inverse problems, it is possible for model parameters to change substantially and still

fit the observations. To date, there has been little discussion concerning the possible variation in non-linear inverse problems that has not involved some type of linearization. In Vasco (1998) a homotopy approach is used to examine the variation due to changes in the weight given to regularization penalty terms in the inversion. In this algorithm the solution is continuously deformed as the regularization weight is varied. The method is useful in constructing trade-off curves for the non-linear inverse problem and determining the regularization penalty weight. In Mosegaard and Tarantola (1995) a sampling algorithm is used to generate a large collection of models according to the posterior probability distribution. This collection of models may be used to explore the range of possible solutions. However, the posterior distribution does depend on which *a priori* information is used in solving the inverse problem.

In the present paper the fit to the data is maintained while the solution is modified in order to minimize or maximize some aspect of the model. This approach is quite general and may be used to minimize model roughness, to minimize the difference between the solution and a prior model, as well as to find bounds on model parameters. While I have applied the method directly to the constraint equations defined by the forward problem, it is possible to work with the normal equations of a least squares formulation. Furthermore, Lie group methods can be applied to the general continuous problems involving differential and integral equations (Olver 1986). As such, it is possible to treat continuous inverse problems directly, without resorting discretization at the outset, as in Vasco (1997). Finally, though the focus of this paper has been on the deterministic approach to inverse problems, Lie group methods should also prove useful in stochastic treatments. For example, group methods could be used to characterize the invariance or symmetry associated with a given probability density function.

The application to the eikonal equation and crosswell tomography illustrates the Lie group approach. In the formulation both the travel times fields associated with each source and the slowness field are treated as unknowns. There are advantages and disadvantages associated with such a treatment. There is greater flexibility and insight when one treats the travel time fields as additional unknowns. For example, it is possible to impose spatial roughness penalties directly on the travel time fields rather than on the slowness distribution. This makes physical sense because one would not expect that the slowness must vary smoothly between a source and receiver. There may be discontinuities due to layering and faults. However, the travel time field must vary continuously in the sub-surface. Thus, it is more appropriate to require the travel time variables to vary smoothly and let the slowness contain discontinuities. In addition, for some inverse problems, such as waveform inversion one may have constraints on the energy in the wavefield. For example, for an artificial source, the wavefield energy cannot exceed the input energy. Therefore, one can bound the energy in the field variables, further constraining the inverse problem. There is additional insight when one includes

both slowness and travel time fields as unknown parameters. For example, it is easy to understand the level of non-uniqueness by counting the total number of equations (16) and the total number of unknowns (17). The primary drawback of including the field variables, such as the travel time fields, is computational. By including a completely new set of variables with each source, the number of unknowns increases rapidly with problem size (number of grid blocks).

The utility of the approach is demonstrated by an application to a pair of crosswell seismic surveys conducted at Lost Hills, California. The application to actual field data illustrates that the algorithm is practical and works in the presence of noise. The application to pre- and post-injection crosswell observations suggests there must be a decrease in seismic velocity in the inter-well region due to CO_2 injection. That is, it is not possible to fit the post-injection observations without some decrease in velocity near the primary injection interval. Furthermore, there is a suggestion that the intersecting fault may act as a conduit for the migration of CO_2 in the subsurface. However, the magnitude of the velocity change along the fault can vary substantially and while remaining compatible with the data.

Acknowledgments.

This work was supported by the Assistant Secretary, Office of Basic Energy Sciences of the U. S. Department of Energy under contract DE-AC03-76SF00098. All computations were carried out at the Center for Computational Seismology and the National Energy Research Computing (NERSC) Center, Berkeley Laboratory.

References

Aki, K., and Richards, P. G., 2002. *Quantitative Seismology*, University Science Books, Sausalito.

Backus, G., 1970. Inference from inadequate and inaccurate data, *Proc. Nat. Acad. Sci. U.S.*, **65**, 1-7.

Backus, G., 1989. Confidence set inference with a prior quadratic bound, *Geophys. J.*, **97**, 119-150.

Backus, G. and Gilbert, F., 1968. The resolving power of gross Earth data, *Geophys. J. R. astr. Soc.*, **16**, 169-205.

Backus, G. and Gilbert, F., 1970. Uniqueness in the inversion of inaccurate gross Earth data, *Phil. Trans. R. Soc. Lond.*, **266A**, 123-192.

Bluman, G. W., and Kumei, S., 1989. *Symmetries and Differential Equations*, Springer-Verlag, New York.

Deal, M. M., and Nolet, G., 1996. Nullspace shuttles, *Geophys. J. Int.*, **124**, 372-380.

Euler, N., and W.-H. Steeb, 1992. *Continuous Symmetries, Lie Algebras and Differential Equations*, Wissenschaftsverlag, Mannheim.

Gill, P. E., Murray, W., and Wright, M. H., 1981. *Practical Optimization*, Academic Press, New York.

Gilmore, R., 1974. *Lie Groups, Lie Algebras, and Some of Their Applications*, Academic Press, New York.

Gritto, R., Daley, T. M., and Myer, L. R., 2004. Joint cross-well and single-well seismic studies of CO_2 injection in an oil reservoir, *Geophysical Prosp.*, **52**, 323-339.

Hoversten, G. M., Gritto, R., Washbourne, J., Daley, T., 2003. Pressure and fluid saturation prediction in a multicomponent reservoir using combined seismic and electromagnetic imaging, *Geophysics*, **68**, 1580-1591.

Jackson, D. D., 1972. Interpretation of inaccurate, insufficient, and inconsistent data, *Geophys. J. R. astr. Soc.*, **28**, 97-109.

Jackson, D. D., 1979. The use of *a priori* data to resolve non-uniqueness in linear inversion, *Geophys. J. R. astr. Soc.*, **57**, 137-157.

Mosegaard, K., and Tarantola, A., 1995. Monte Carlo sampling of solutions to inverse problems, *J. Geophys. Res.*, **100**, 12431-12447.

Noble, B., and Daniel, J. W., 1977. *Applied Linear Algebra*, Prentice-Hall, Englewood Cliffs, New Jersey.

Olver, P. J., 1986. *Applications of Lie Groups to Differential Equations*, Springer-Verlag, New York.

Parker, R., 1974. Best bounds on density and depth from gravity data, *Geophysics*, **39**, 644-649.

Parker, R. L., 1994. *Geophysical Inverse Theory*, Princeton University Press, Princeton, New Jersey.

Press, F., 1968. Earth models obtained by Monte Carlo inversion, *J. Geophys. Res.*, **73**, 5223-5234.

Rowbotham, P. S., and Pratt, R. G., 1997. Improved inversion through the use of the null space, *Geophysics*, **62**, 869-883.

Sabatier, P. C., 1977. Positivity constraints in linear inverse problems - I. General theory, *Geophys. J. R. astr. Soc.*, **48**, 415-441.

Safon, C., Vasseur, G., and Cuer, M., 1977. Some applications of linear programming to the inverse gravity problem, *Geophysics*, **42**, 1215-1229.

Sambridge, M., 1998. Exploring multi-dimensional landscapes without a map, *Inverse Problems*, **14**, 427-440.

Stark, P. B., 1992. Inference of infinite-dimensional inverse problems: Discretization and duality, *J. Geophys. Res.*, **97**, 14055-14082.

Tarantola, A., 1987. *Inverse Problem Theory*, Elsevier, Amsterdam.

Vasco, D. W., 1995. A transformational approach to geophysical inverse problems, *Geophys. J. Int.*, **123**, 183-212.

Vasco, D. W., 1997. Groups, algebras, and the non-linearity of geophysical inverse problems, *Geophys. J. Int.*, **131**, 9-23.

Vasco, D. W., 1998. Regularization and trade-off associated with nonlinear geophysical inverse problems: penalty homotopies, *Inverse Problems*, **14**, 1033-1052.

Vasco, D. W., 1999. Intersections, ideals, and inversion, *Inverse Problems*, **15**, 1573-1602.

Vasco, D. W., 2000. An algebraic formulation of geophysical inverse problems, *Geophys. J. Int.*, **142**, 970-990.

Wiggins, R. A., 1972. The general linear inverse problem: implication of surface waves and free oscillations for Earth structure, *Rev. Geophys. Space. Phys.*, **10**, 251-285.

D. W. Vasco, Earth Sciences Division, Berkeley Laboratory, 1 Cyclotron Road, Berkeley, CA 94720. (e-mail: dwvasco@lbl.gov)

Received 2005

Figure 1. Reference slowness model used to generate travel times for a synthetic test. The five sources are denoted by stars at the left side of the model. The fourteen receivers are denoted by filled squares and are found on the right-hand-side of the model. The grey-scale represents the slowness variation in the crosswell region.

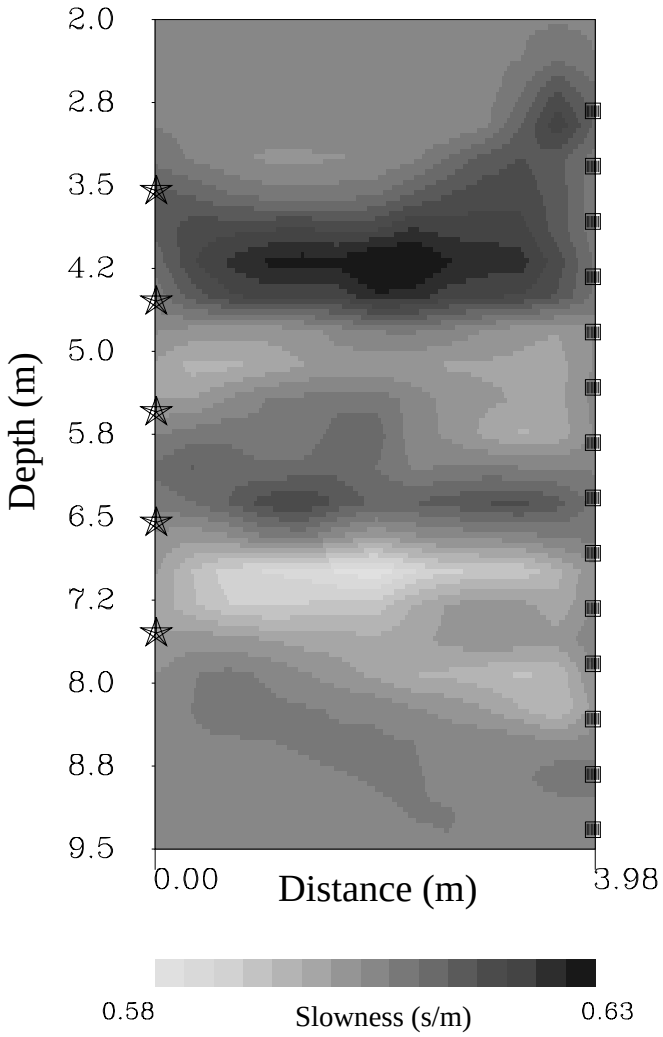
2.0
2.8
3.5
4.2
5.0
5.8
6.5
7.2
8.0
8.8
9.5
Depth (m)
0.00
Distance (m)
3.98
0.58
Slowness (s/m)
0.63

Figure 2. Three travel time fields associated with sources 1, 3, and 5. The contours and grey-scale display the travel time fields for the three sources and the model shown in Figure 1.

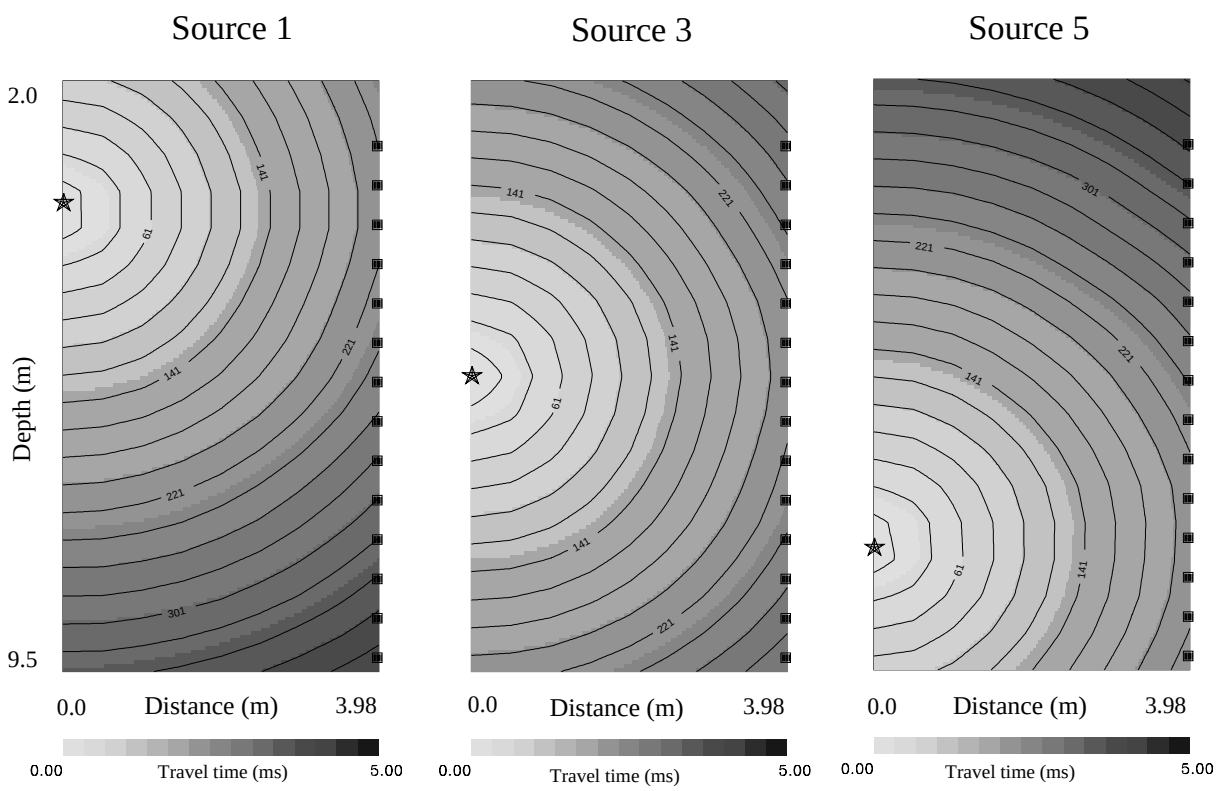

CONTOUR FROM 0.10000E-01 TO 4.6100 CONTOUR INTERVAL OF 0.20000 PT(3,3)= 3.3014 LABELS SCALED BY 0.10000E-01

CONTOUR FROM 0.10000E-01 TO 4.6100 CONTOUR INTERVAL OF 0.20000 PT(3,3)= 2.0745 LABELS SCALED BY 10.00

CONTOUR FROM 0.10000E-01 TO 4.6100 CONTOUR INTERVAL OF 0.20000 PT(3,3)= 0.85819 LABELS SCALED BY 100.00

Figure 3. (Left) Unit vectors in the direction of the gradient of the travel time field associated with source 3. (Right) The square root of the magnitude of the gradient vectors.

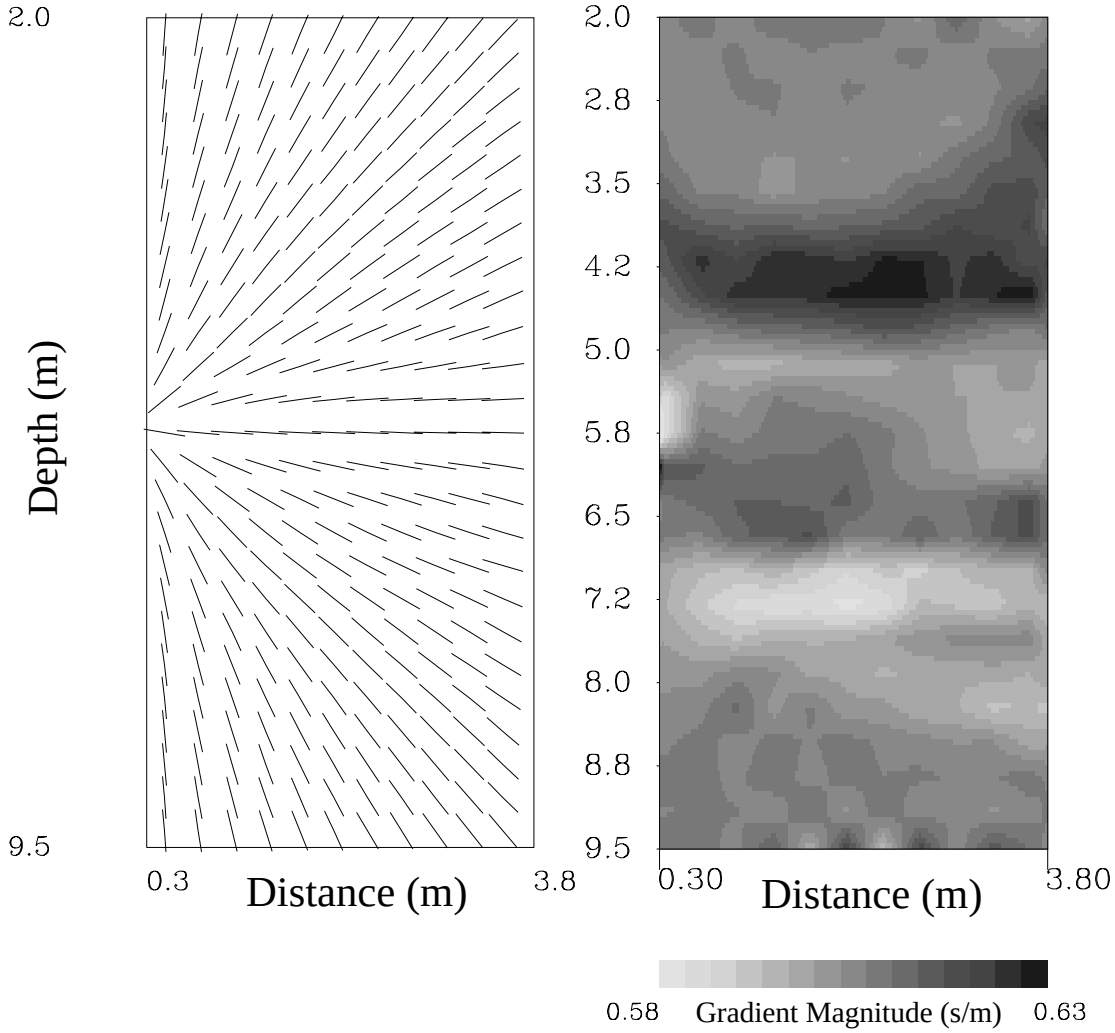
2.0
9.5
Depth (m)
0.3
Distance (m)
3.8
2.0
2.8
3.5
4.2
5.0
5.8
6.5
7.2
8.0
8.8
9.5
0.30
Distance (m)
3.80
0.58
Gradient Magnitude (s/m)
0.63

Figure 4. Singular values associated with a singular value decomposition (SVD) of the matrix **P** in equation (23).

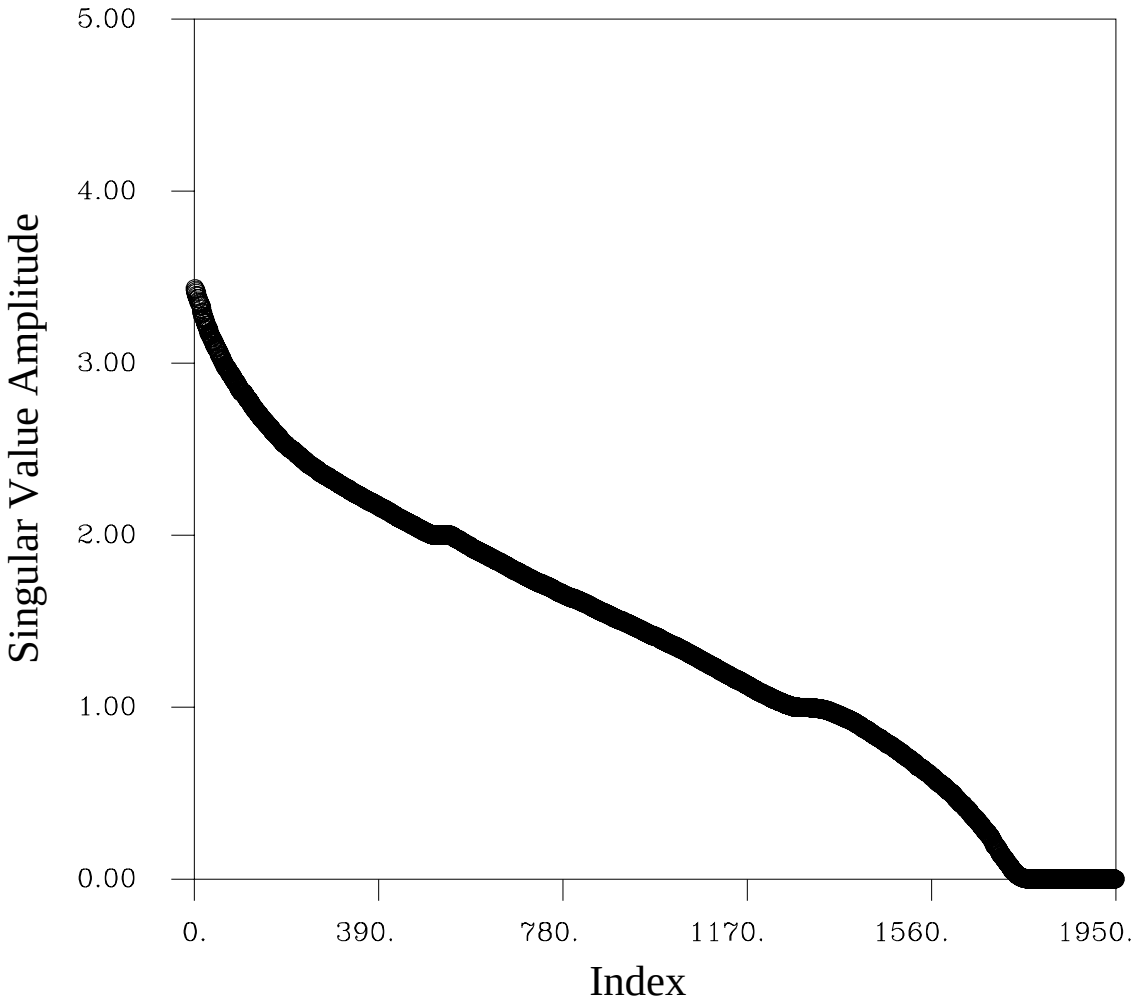

Figure 5. Three singular vectors corresponding to the SVD of the matrix $\mathbf{P}$. The components of the 1st, 6th, and 25th singular vectors corresponding to the arrival time field of source 1, $\mathbf{u}^1$, and the square of the slowness σ. The magnitude of the vector components are plotted in the cells to which they correspond. The grey-scale denotes the magnitude of each component.

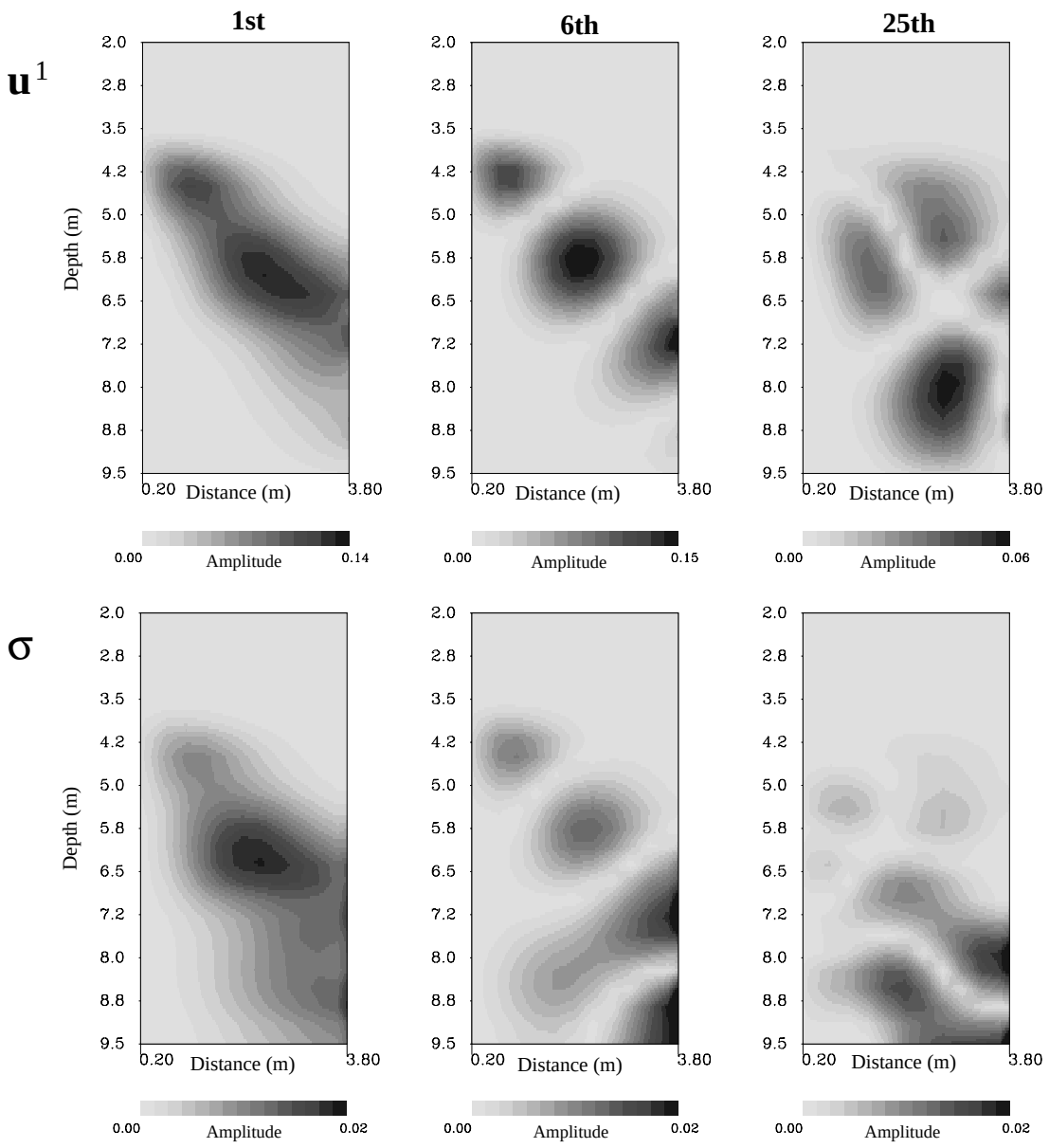
1st
6th
25th
u 1
σ
Depth (m)
2.0
2.8
3.5
4.2
5.0
5.8
6.5
7.2
8.0
8.8
9.5
0.20
Distance (m)
3.80
0.00
Amplitude
0.14
0.15
0.06
0.02

Figure 6. Grey-scale plot of selected components of the singular vector associated with the largest singular value. The components correspond to the 1st, 3rd, and 5th sources, $\mathbf{u}^1$, $\mathbf{u}^3$, and $\mathbf{u}^5$, respectively.

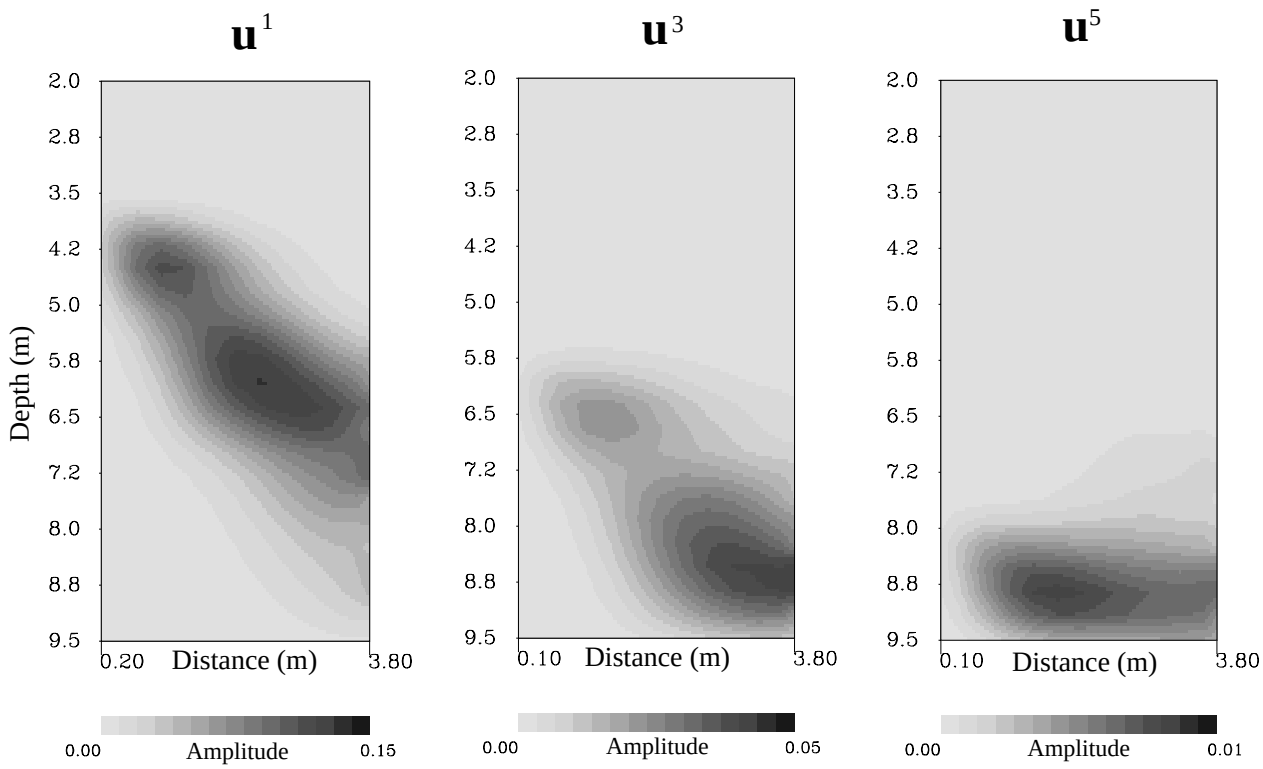
u 1
u 3
u 5
Depth (m)
2.0
2.8
3.5
4.2
5.0
5.8
6.5
7.2
8.0
8.8
9.5
0.20
0.10
0.10
Distance (m)
3.80
Amplitude
0.00
0.15
0.05
0.01

Figure 7. Three null vectors corresponding to the SVD of the matrix $\mathbf{P}$. The components of the 1st, 50th, and 100th null vectors corresponding to the arrival time field of source 1, $\mathbf{u}^1$, and the square of the slowness σ. The grey-scale denotes the value, plotted in the cell that corresponds to the particular vector component.

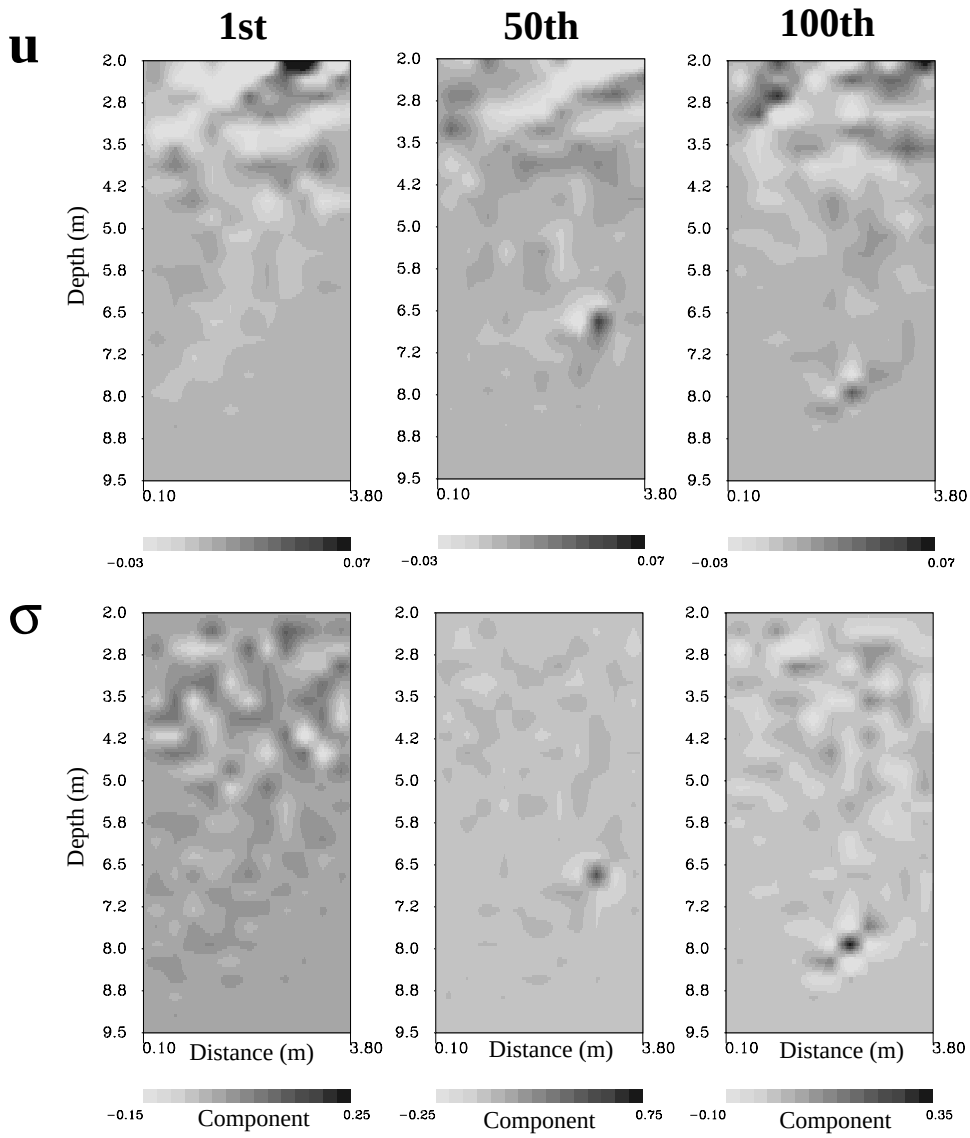
u
1st
50th
100th
Depth (m)
2.0
2.8
3.5
4.2
5.0
5.8
6.5
7.2
8.0
8.8
9.5
0.10
3.80
−0.03
0.07
σ
Distance (m)
−0.15
Component
0.25
−0.25
0.75
−0.10
0.35

Figure 8. A plot of the function $R(\mathbf{a}) = (\mathbf{x}' - \mathbf{\Pi})^T \cdot (\mathbf{x}' - \mathbf{\Pi})$ as a function of the number of iterations, where $\mathbf{\Pi}$ is associated with a uniform background value of 0.61 s/km.

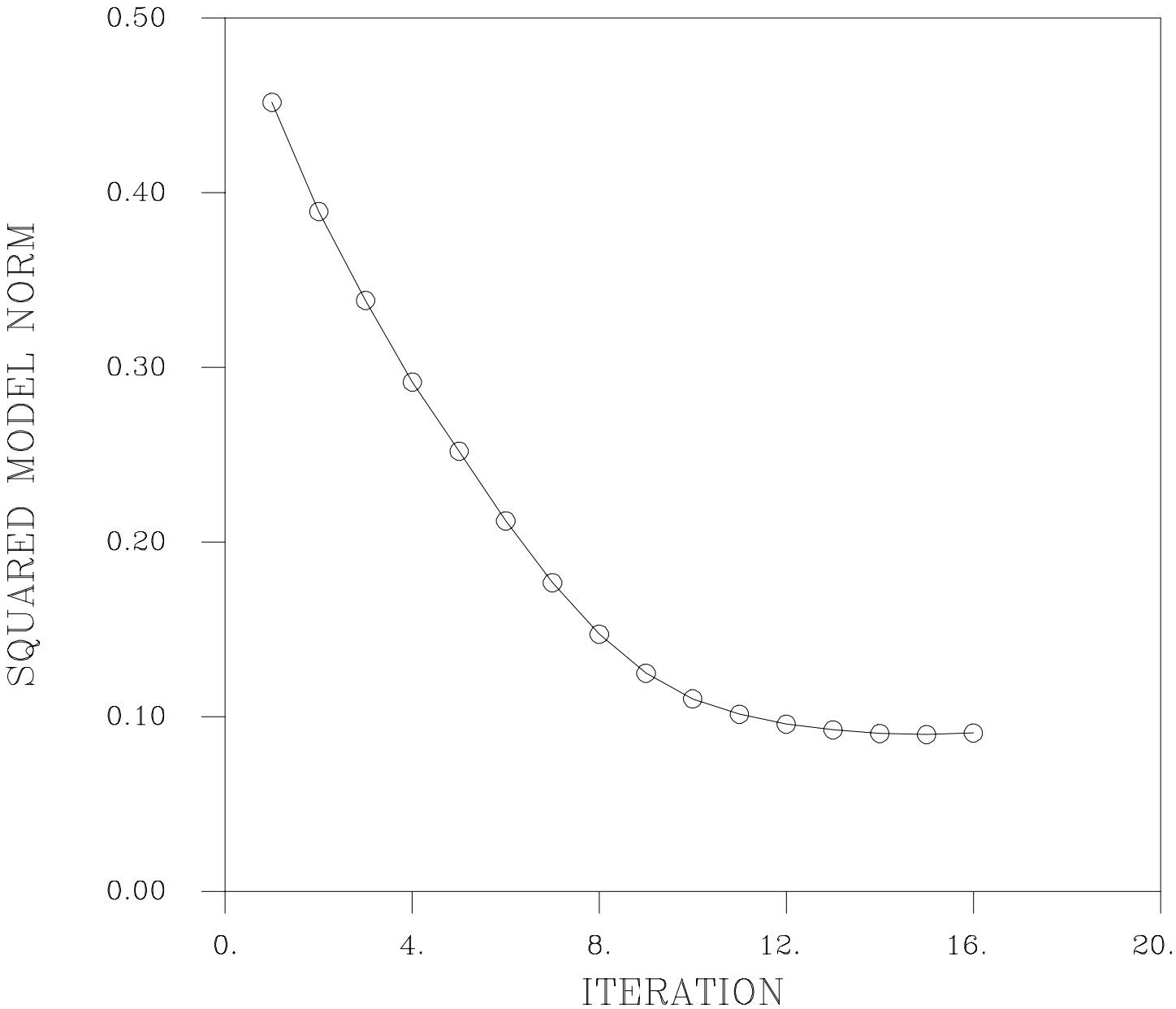

Figure 9. The slowness distribution after 0, 4, 8, and 16 updates. The updates, given according to equation (32), are designed to minimize the function $R(\mathbf{a})$ defined by equation (31).

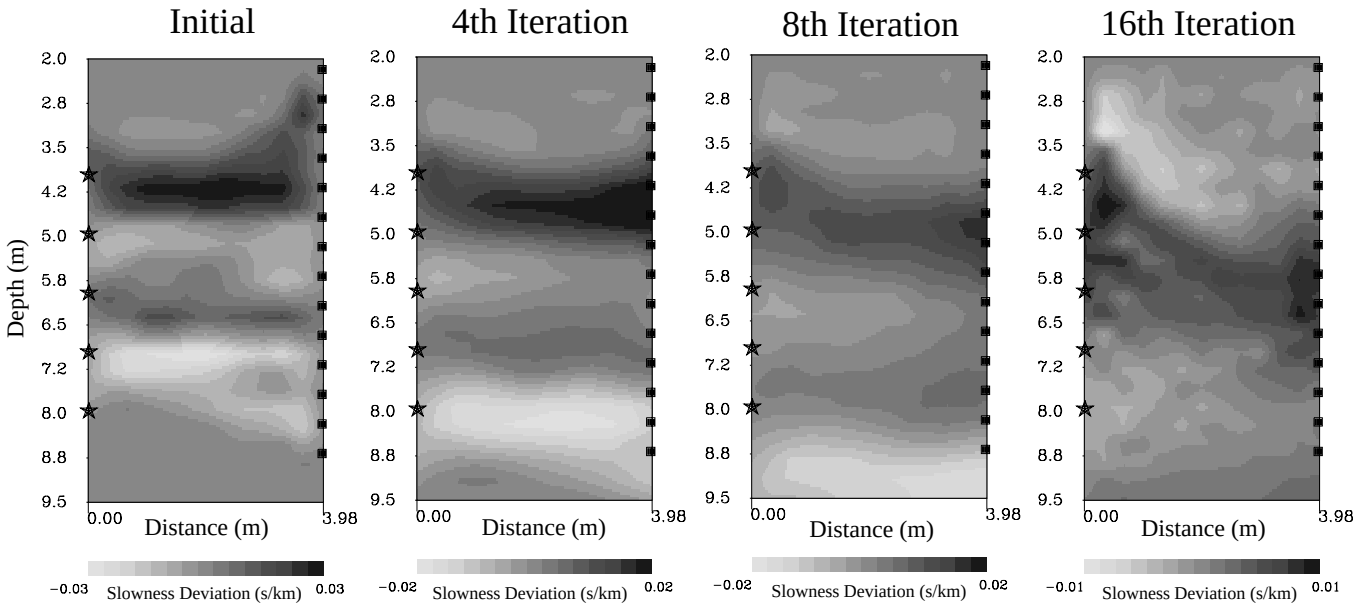
Initial
4th Iteration
8th Iteration
16th Iteration
Depth (m)
2.0
2.8
3.5
4.2
5.0
5.8
6.5
7.2
8.0
8.8
9.5
0.00
3.98
Distance (m)
−0.03
0.03
−0.02
0.02
−0.01
0.01
Slowness Deviation (s/km)

Figure 10. Calculated travel times plotted against reference travel times after 0, 4, 8, and 16 updates. For a perfect match to the synthetic values the points would lie on the solid diagonal line.

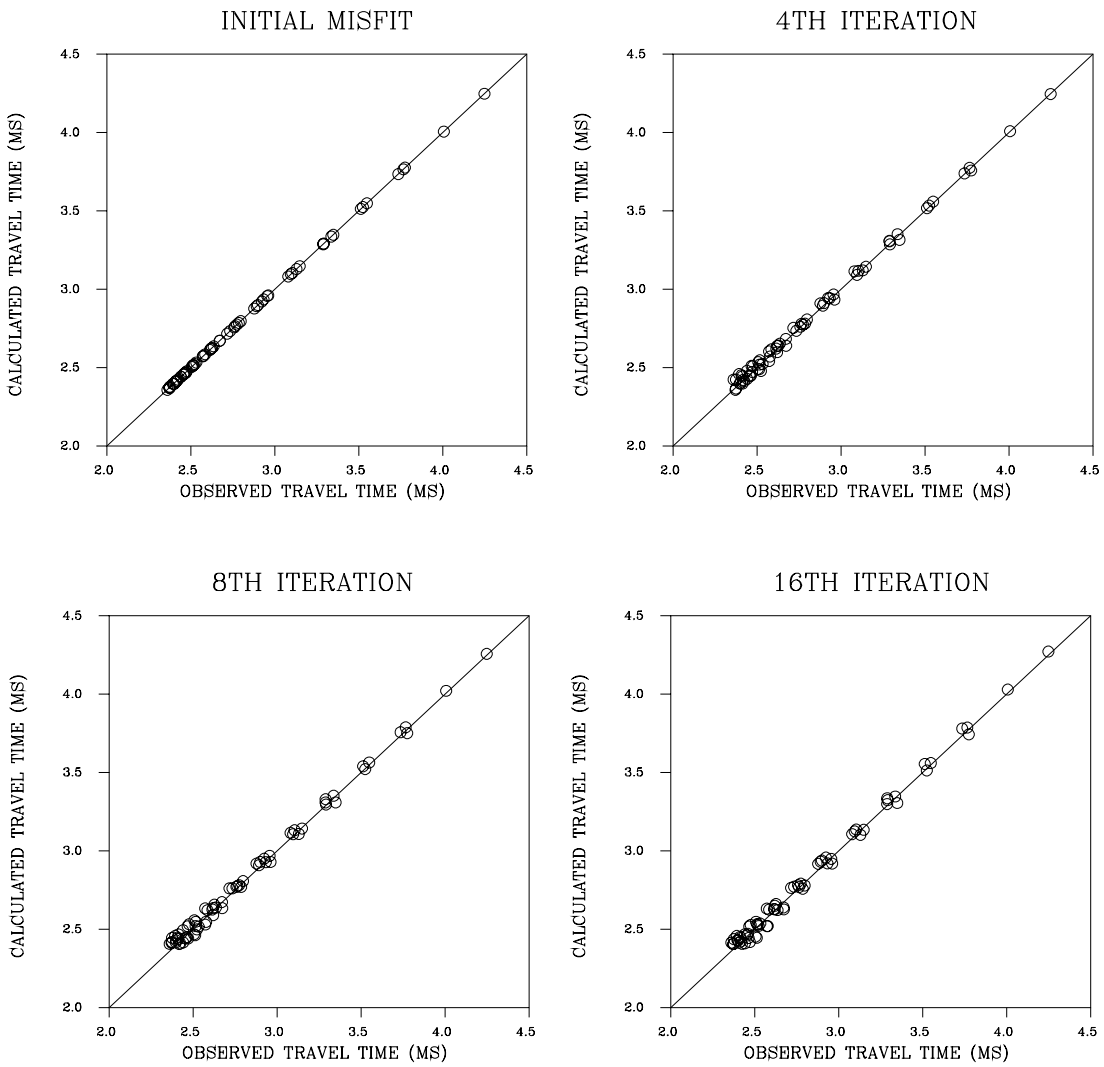
INITIAL MISFIT
4TH ITERATION
8TH ITERATION
16TH ITERATION
CALCULATED TRAVEL TIME (MS)
OBSERVED TRAVEL TIME (MS)
2.0
2.5
3.0
3.5
4.0
4.5

Figure 11. Layout of the monitoring experiment at the Lost Hills oil field. The two fiber-glass cased observation wells (OB-C1 and OB-C2) are denoted by filled squares. The injection well 11-8WR is denoted by an open circle.

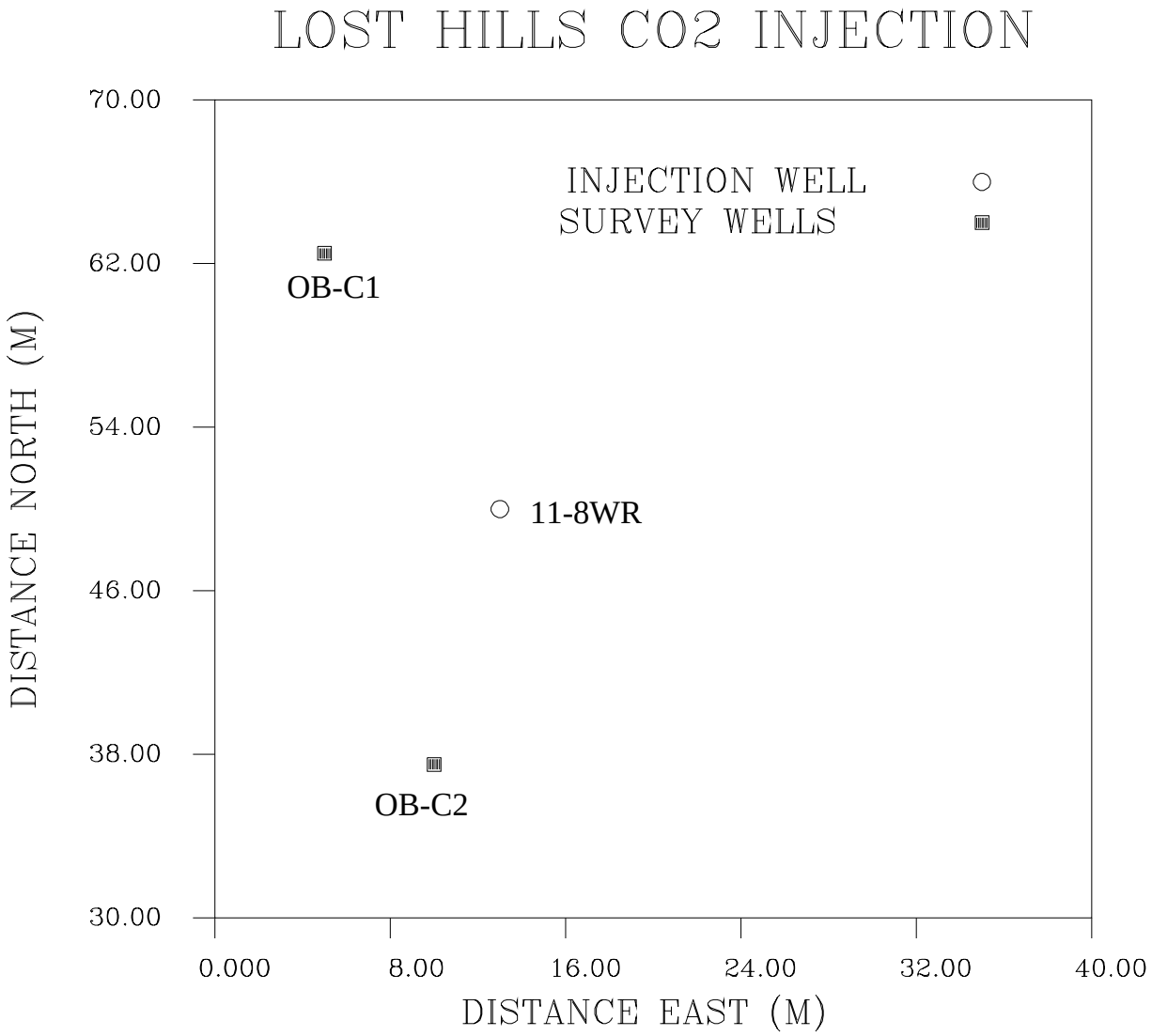
LOST HILLS CO2 INJECTION
INJECTION WELL
SURVEY WELLS
OB-C1
11-8WR
OB-C2
70.00
62.00
54.00
46.00
38.00
30.00
DISTANCE NORTH (M)
0.000
8.00
16.00
24.00
32.00
40.00
DISTANCE EAST (M)

Figure 12. Ray coverage for the pre- and post-injection crosswell seismic surveys. The grey-scale depicts the ray density, the number of rays per cell, in the interwell region.

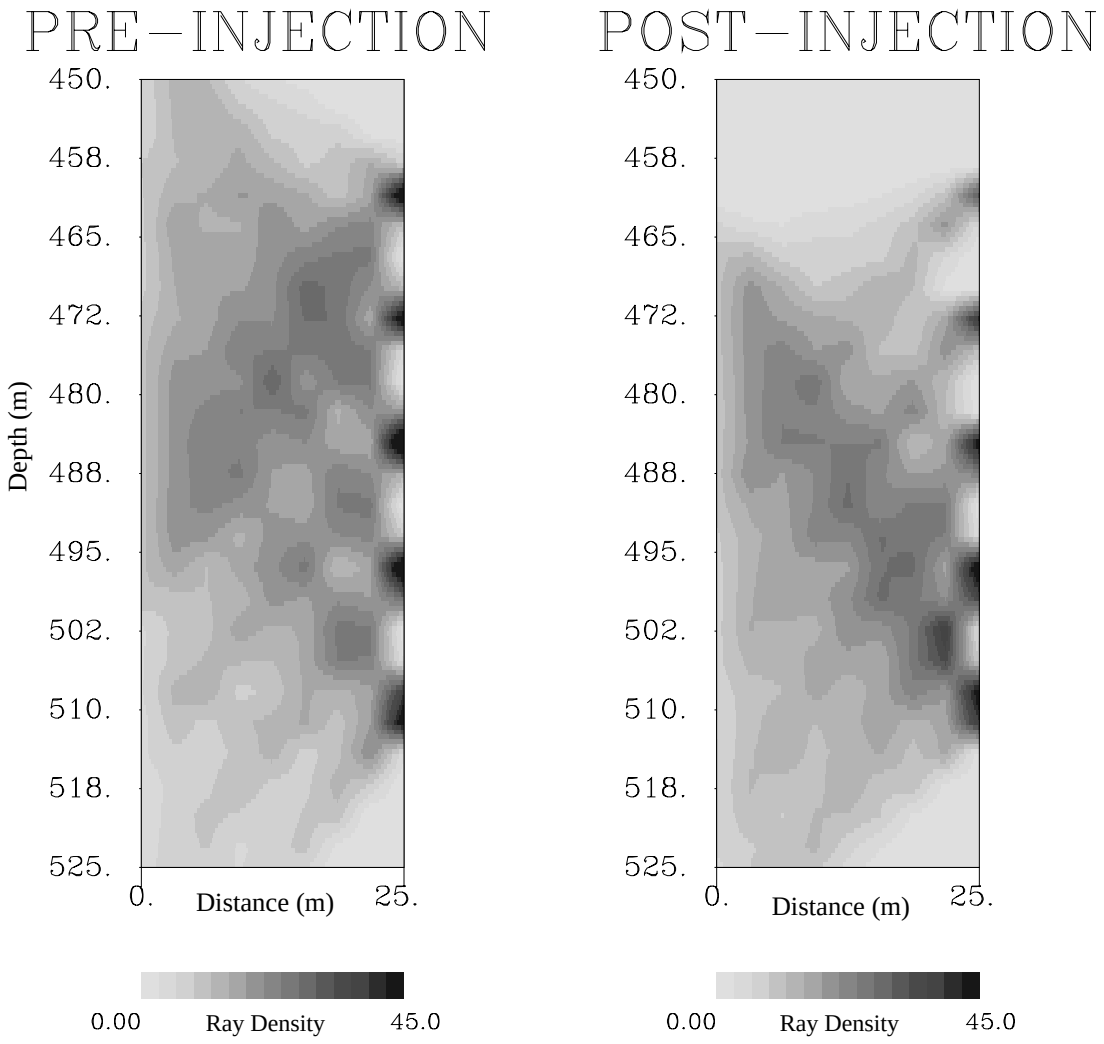

Figure 13. Plot of travel times as a function of source and receiver offset. The open circles are the observed travel times and the filled squares are the travel times calculated using a uniform velocity model (1.72 km/s).

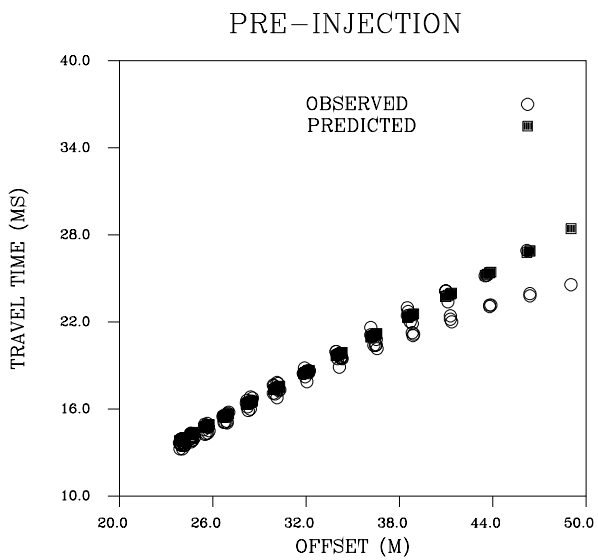
PRE−INJECTION
OBSERVED
PREDICTED
TRAVEL TIME (MS)
OFFSET (M)
40.0
34.0
28.0
22.0
16.0
10.0
20.0
26.0
32.0
38.0
44.0
50.0

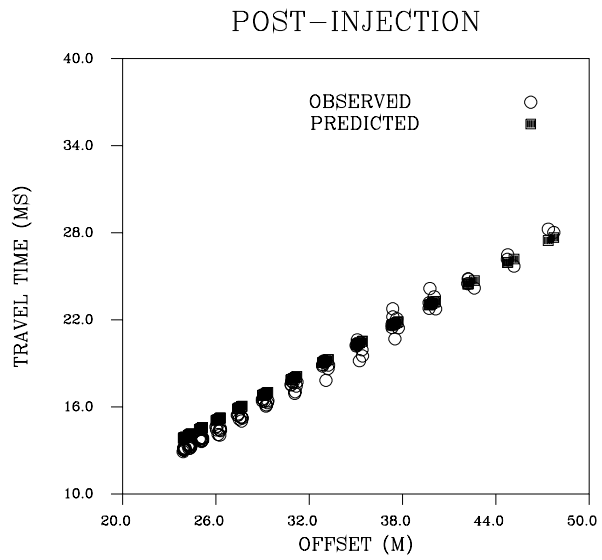
POST−INJECTION
OBSERVED
PREDICTED
TRAVEL TIME (MS)
OFFSET (M)
40.0
34.0
28.0
22.0
16.0
10.0
20.0
26.0
32.0
38.0
44.0
50.0

Figure 14. Velocity variations which resulted from an inversion of pre- and post-injection arrival time data. The heterogeneity is plotted as deviations from a uniform background velocity of 1.72 km/s.

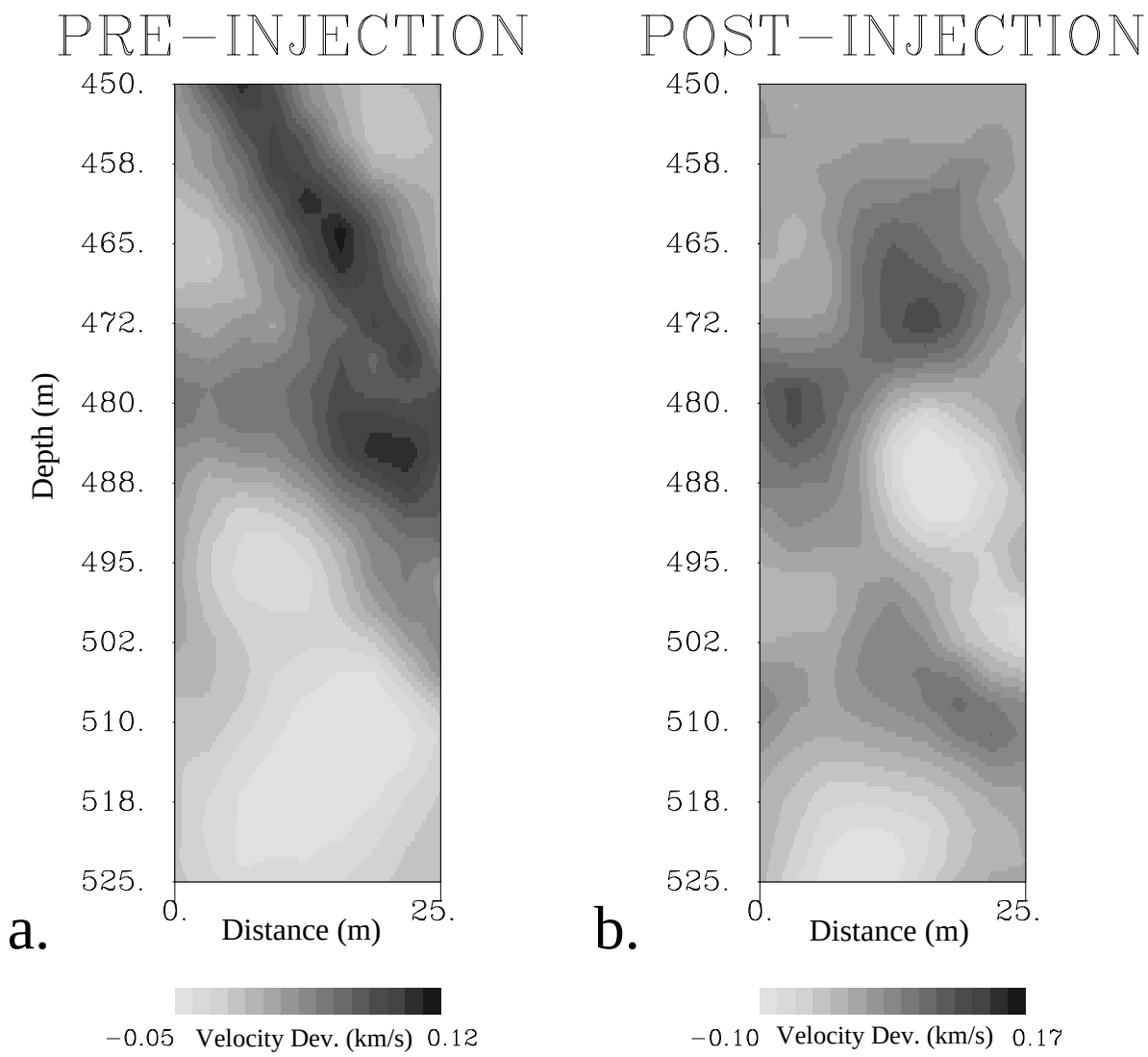
PRE−INJECTION
POST−INJECTION
450.
458.
465.
472.
480.
488.
495.
502.
510.
518.
525.
Depth (m)
0.
25.
Distance (m)
a.
b.
−0.05
Velocity Dev. (km/s)
0.12
−0.10
Velocity Dev. (km/s)
0.17

Figure 15. A difference tomogram representing velocity changes which occurred during the injection of CO_2. The difference tomogram is formed by simply subtracting the pre-injection velocities from the post-injection velocities. Three injection points, signifying the locations of injection intervals in well 11-8WR in Figure 11, are indicated by the filled squares. The well 11-8WR is approximately six meters out of the plane containing the observation wells. The size of each square is proportional to the volume of injected CO_2.

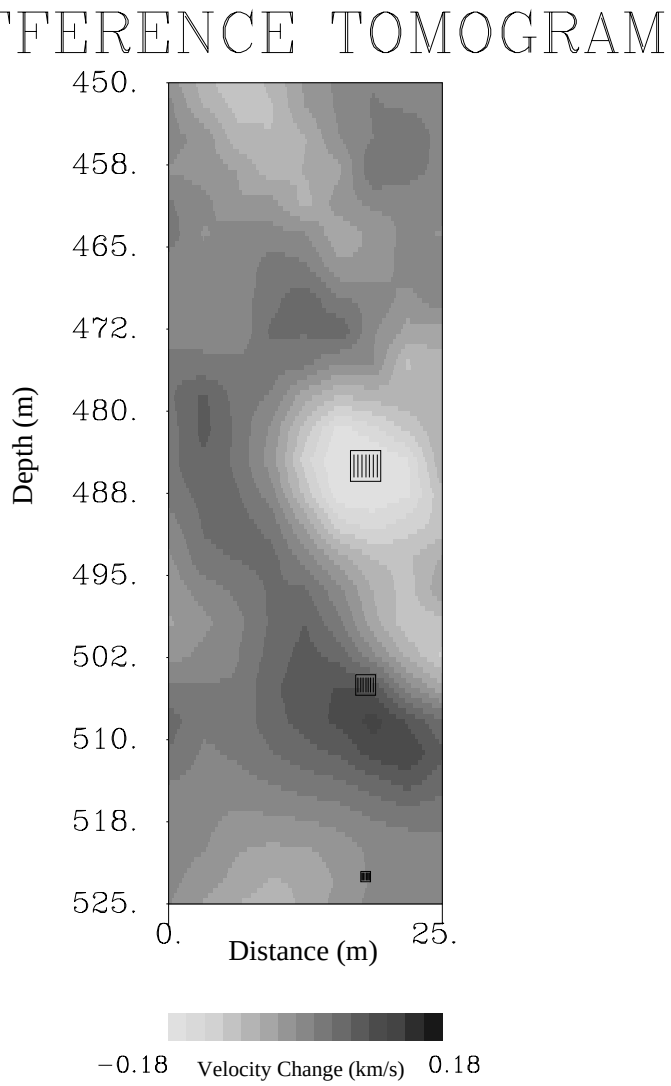
DIFFERENCE TOMOGRAM
450.
458.
465.
472.
480.
488.
495.
502.
510.
518.
525.
Depth (m)
0.
25.
Distance (m)
−0.18
Velocity Change (km/s)
0.18

Figure 16. A plot of the variation of $R(\mathbf{a}) = (\mathbf{x}' - \mathbf{\Pi})^T \cdot (\mathbf{x}' - \mathbf{\Pi})$ as a function of the number of iterations. The model $\mathbf{\Pi}$ corresponds to the pre-injection velocity variation shown in Figure 14a. In essence, I am trying to make the post-injection velocity model resemble the pre-injection velocity model. Stated another way, I am trying to make the difference tomogram as small as possible while satisfying the observations.

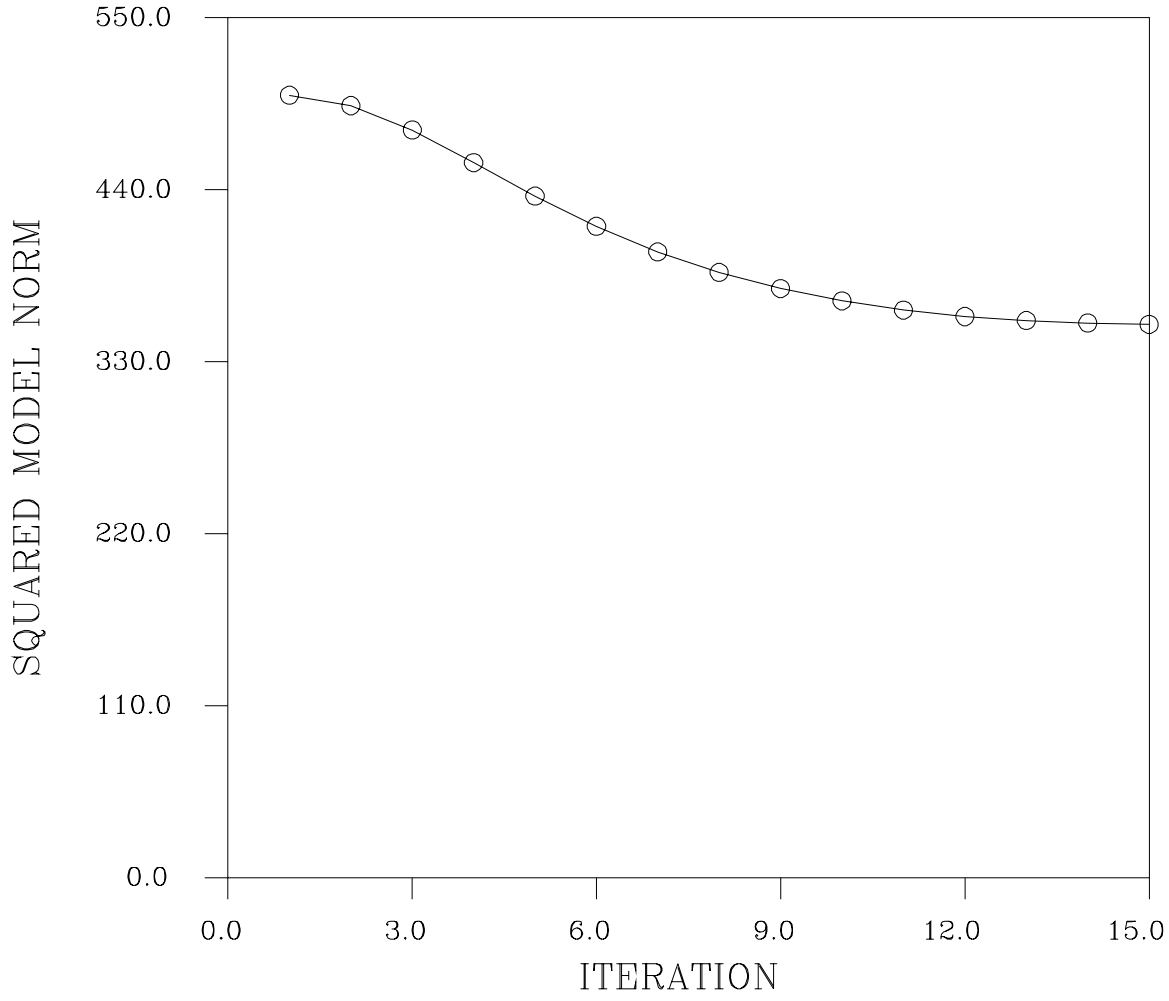
550.0
440.0
330.0
220.0
110.0
0.0
SQUARED MODEL NORM
0.0
3.0
6.0
9.0
12.0
15.0
ITERATION

Figure 17. Post-injection velocity deviations from a uniform background value 0f 1.72 km/s. The velocity deviations correspond to the 5th, 10th, and 15th iterations of the Lie group algorithm. The updates are given by equation (32), as discussed in the text.

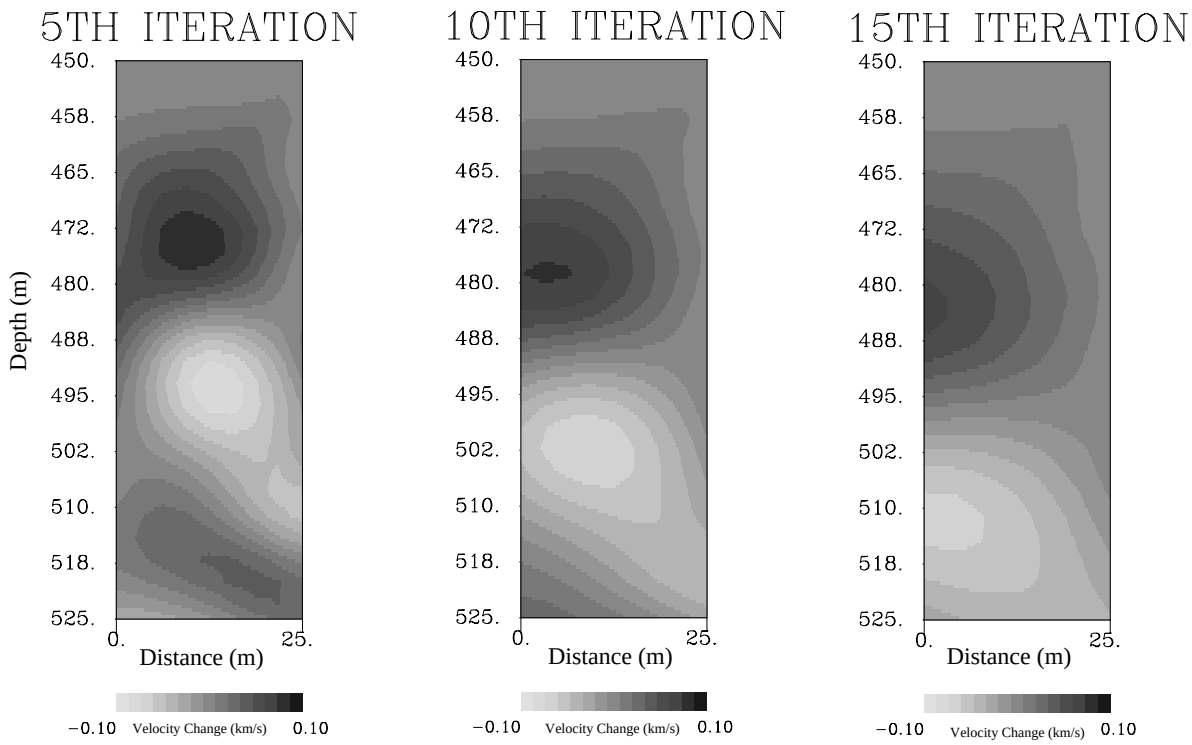
5TH ITERATION
10TH ITERATION
15TH ITERATION
Depth (m)
450.
458.
465.
472.
480.
488.
495.
502.
510.
518.
525.
0.
25.
Distance (m)
−0.10
Velocity Change (km/s)
0.10

Figure 18. The difference tomogram obtained by subtracting the pre-injection model shown in Figure 14a from the post-injection model which resulted from the Lie group algorithm. The final post-injection model is the 15th iteration, shown in Figure 17.

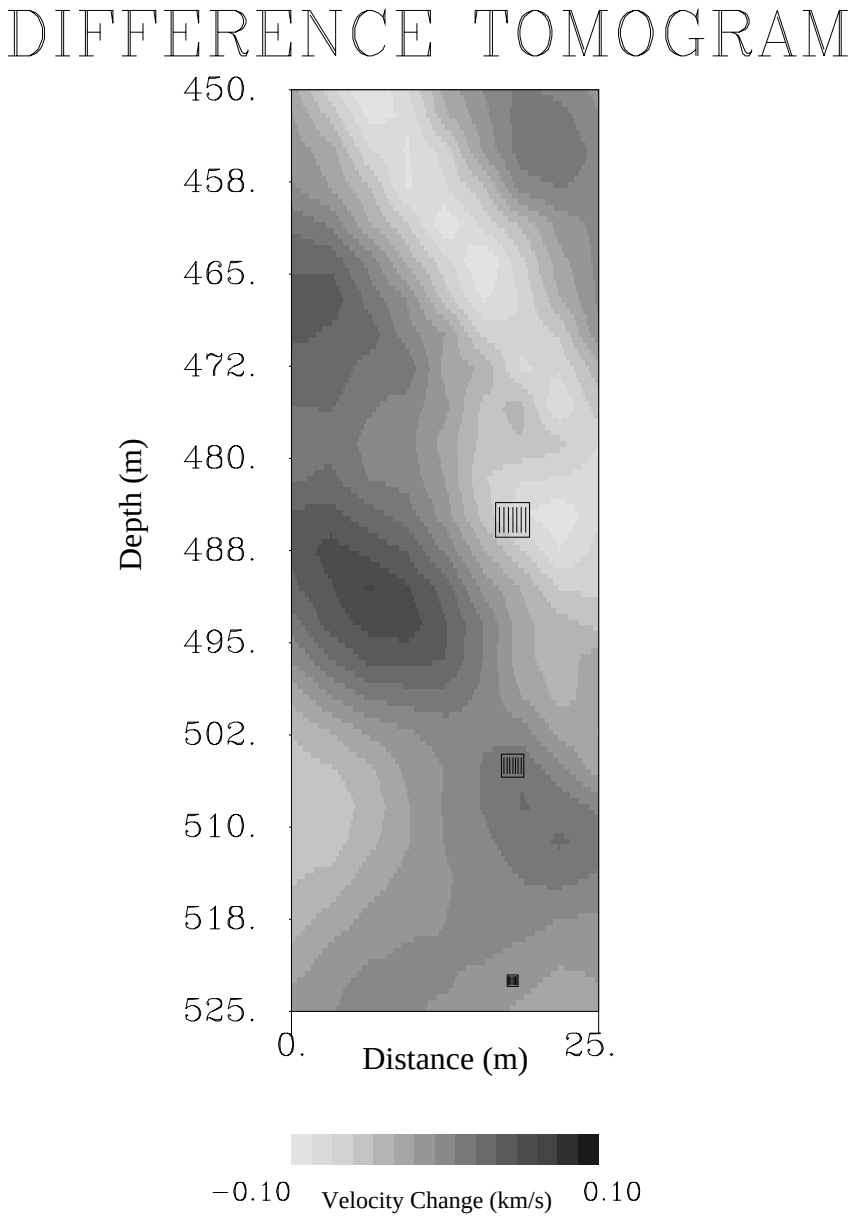
DIFFERENCE TOMOGRAM
450.
458.
465.
472.
480.
488.
495.
502.
510.
518.
525.
Depth (m)
0.
25.
Distance (m)
−0.10
Velocity Change (km/s)
0.10

Figure 19. The initial and final travel time matches for the Lost Hills post-injection inversion. The travel times calculated using the initial (Figure 14b) and final (Figure 17) post-injection models of the iterative algorithm.

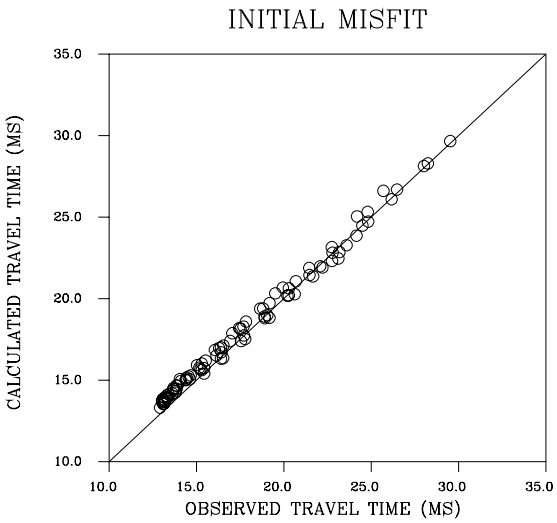
INITIAL MISFIT
CALCULATED TRAVEL TIME (MS)
OBSERVED TRAVEL TIME (MS)
10.0
15.0
20.0
25.0
30.0
35.0

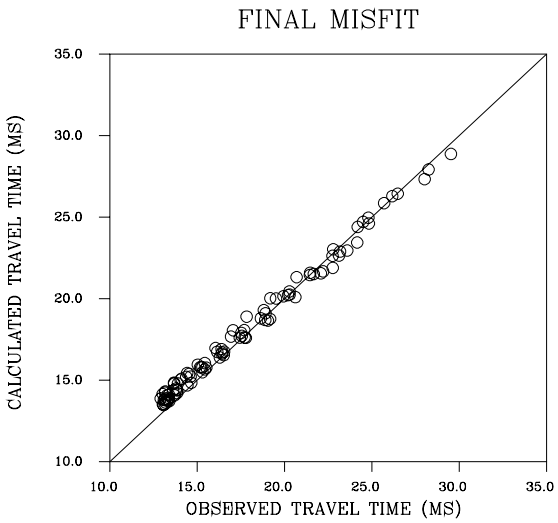
FINAL MISFIT
CALCULATED TRAVEL TIME (MS)
OBSERVED TRAVEL TIME (MS)
10.0
15.0
20.0
25.0
30.0
35.0